การสังเคราะห์เพอรอฟสไกต์เมมเบรนความหนาแน่นสูงชนิด $(La, Ba)_{1-x}Sr_xCo_{1-y}Fe_yO_{3-\delta}$ และสมบัติการซึมผ่านของออกซิเจน

นายนิติพงษ์ จิราทิวัฒนากุล

วิทยานิพนธ์นี้เป็นส่วนหนึ่งของการศึกษาตามหลักสูตรปริญญาวิทยาศาสตรมหาบัณฑิต
สาขาวิชาเคมี ภาควิชาเคมี
คณะวิทยาศาสตร์ จุฬาลงกรณ์มหาวิทยาลัย
ปีการศึกษา 2547

ISBN 974-53-1541-9

ลิขสิทธิ์ของจุฬาลงกรณ์มหาวิทยาลัย

SYNTHESIS OF DENSE PEROVSKITE MEMBRANE $(La, Ba)_{1-x}Sr_xCo_{1-y}Fe_yO_{3-\delta}$ AND THEIR OXYGEN PERMEATION PROPERTY

Mr. Nitiphong Jirathiwathanakul

A Thesis Submitted in Partial Fulfillment of the Requirements
for the Degree of Master of Science in Chemistry
Department of Chemistry
Faculty of Science
Chulalongkorn University
Academic year 2004

ISBN 974-53-1541-9

Thesis Title SYNTHESIS OF DENSE PEROVSKITE MEMBRANE $(La, Ba)_{1-x}Sr_xCo_{1-y}Fe_yO_{3-\delta}$ AND THEIR OXYGEN PERMEATION PROPERTY

By Mr. Nitiphong Jirathiwathanakul

Field of Study Chemistry

Thesis Advisor Oravan Sanguanruang, Ph.D.

Accepted by the Faculty of Science, Chulalongkorn University in Partial Fulfillment of the Requirements for the Master's Degree

………………………………… Dean of the Faculty of Science
(Professor Piamsak Menasveta, Ph.D.)

THESIS COMMITTEE

………………………………… Chairman
(Associate Professor Sirirat Kokpol, Ph.D.)

………………………………… Thesis Advisor
(Oravan Sanguanruang, Ph.D.)

………………………………… Member
(Associate Professor Supawan Tantayanon, Ph.D.)

………………………………… Member
(Nipaka Sukpirom, Ph.D.)

นายนิติพงษ์ จิราทิวัฒนากุล : การสังเคราะห์เพอรอฟสไกต์เมมเบรนความหนาแน่นสูงชนิด $(La, Ba)_{1-x}Sr_xCo_{1-y}Fe_yO_{3-\delta}$ และสมบัติการซึมผ่านของออกซิเจน
(SYNTHESIS OF DENSE PEROVSKITE MEMBRANE $(La, Ba)_{1-x}Sr_xCo_{1-y}Fe_yO_{3-\delta}$ AND THEIR OXYGEN PERMEATION PROPERTY)
อาจารย์ที่ปรึกษา: ดร. อรวรรณ สงวนเรือง, 70 หน้า, ISBN 974-53-1541-9

สังเคราะห์ $La_{1-x}Sr_xCo_{1-y}Fe_yO_{3-\delta}$ (LSCF) และ $Ba_{1-x}Sr_xCo_{1-y}Fe_yO_{3-\delta}$ (BSCF) เมื่อ x เท่ากับ 0.2-0.5 และ y เท่ากับ 0.1-0.5 ด้วยวิธีซิเทรตและซิเทรตประยุกต์ตามลำดับ สารดังกล่าวเป็นวัตถุดิบในการผลิตเป็นเมมเบรนเพื่อใช้แยกก๊าซออกซิเจนจากอากาศ นำผงเพอรอฟสไกต์มาขึ้นรูปเป็นเมมเบรนด้วยเครื่องอัดด้านเดียวและซินเทอริงที่อุณหภูมิ 1,100-1,300 °C เป็นเวลา 10 ชั่วโมง ตรวจสอบสารประกอบเพอรอฟสไกต์ออกไซด์ทั้ง LSCF และ BSCF ด้วยเทคนิคเลี้ยวเบนของรังสีเอ็กซ์ เทคนิคสแกนนิงอิเล็กโตรไมโครสโคปี วัดสมบัติการซึมผ่านของออกซิเจนด้วย TGA และ O_2-TPD จากเทคนิคเลี้ยวเบนของรังสีเอ็กซ์พบว่า LSCFเป็นโครงสร้างผลึกเดียวของเพอรอฟสไกต์เมื่อค่า x อยู่ในช่วง 0.2-0.3 และเกิดสารประกอบ $SrCO_3$ เมื่อค่า x มากกว่า 0.3 ขึ้นไป อย่างไรก็ตาม $SrCO_3$ จะหายไปหลังการทำซินเทอริงที่อุณหภูมิ 1,300°C ในกรณีของ BSCF ผลการวิเคราะห์ด้วยเทคนิคเลี้ยวเบนรังสีเอกซ์ เกิด $BaFeO_{2.9}$ ขึ้นเมื่อค่า y น้อยกว่าหรือเท่ากับ 0.2 ผลที่ได้แสดงว่าปริมาณของสตรอนเทียมและ โคบอลต์ที่น้อย ในระบบของ LSCF และ BSCF เป็นสาเหตุที่เกิดโครงสร้างชนิดรอมโบฮีดรอลและคิวบิกตามลำดับ เมมเบรนที่มีความหนาแน่นสูงเตรียมได้จากวิธีการสังเคราะห์และอุณหภูมิซินเทอริงที่เหมาะสม จากการวิเคราะห์ด้วย TGA แสดงให้เห็นว่าในระบบ LSCF มีตำแหน่งที่ว่างของออกซิเจนเพิ่มขึ้นเมื่อปริมาณสตรอนเทียมเพิ่มขึ้นแต่ปริมาณของเหล็กไม่ส่งผลต่อที่ว่างของออกซิเจน ในทางตรงกันข้ามการแทนที่ของสตรอนเทียมในระบบ BSCF ไม่ส่งผลต่อที่ว่างของออกซิเจนแต่เมื่อปริมาณเหล็กลดลง แต่มีผลให้ตำแหน่งที่ว่างของออกซิเจนเพิ่มขึ้น ผลการทดลองของ O_2-TPD ในช่วงอุณหภูมิ 500-800°C แสดงให้เห็นว่าปริมาณการคายออกของออกซิเจนใน LSCF8264 มีค่ามากกว่าใน BSCF8264

ภาควิชา เคมี ลายมือชื่อนิสิต
สาขาวิชา เคมี ลายมือชื่ออาจารย์ที่ปรึกษา
ปีการศึกษา 2547

4572343723: MAJOR CHEMISTRY
KEY WORD: PEROVSKITE, LSCF, BSCF, OXYGEN PERMEATION PROPERTY

MR. NITIPHONG JIRATHIWATHANAKUL : SYNTHESIS OF DENSE PEROVSKITE MEMBRANE (La, Ba)$_{1-x}$Sr$_x$Co$_{1-y}$ Fe$_y$O$_{3-\delta}$ AND THEIR OXYGEN PERMEATION PROPERTY
THESIS ADVISOR : ORAVAN SANGUANRUANG, Ph.D., 70 pp., ISBN 974-53-1541-9

$La_{1-x}Sr_xCo_{1-y}Fe_yO_{3-\delta}$ (LSCF) and $Ba_{1-x}Sr_xCo_{1-y}Fe_yO_{3-\delta}$ (BSCF), where $x = 0.2$-0.5; $y = 0.1$-0.5, have been prepared by citrate and modified citrate methods, respectively. They were the candidate materials for oxygen permeation membrane for air separation. The membranes were prepared by pressing the perovskite powder using a uniaxial peressing machine and sintering around 1,100-1,300°C for 10 hours. LSCF and BSCF perovskite oxides were characterized by X-ray diffraction (XRD), scanning electron microscopy (SEM). Oxygen permeation property was determined by thermogravimetric analysis (TGA) and oxygen temperature-programmed desorption (O_2-TPD). XRD patterns revealed the presence of a single phase of LSCF for substitutions $0.2 \leq x \leq 0.3$. $SrCO_3$ was observed for $x > 0.3$, however it disappeared after sintering at 1,300°C. For BSCF series, the XRD analysis shows $BaFeO_{2.9}$ phase when $y \leq 0.2$. The results indicated that low amount of Sr and Co in the matrix of LSCF and BSCF caused the formation of single rhombohedral and cubic structure, respectively. The dense membranes were obtained from the suitable of the preparation methods and sintering temperature. From TGA, it can be inferred that the oxygen deficiencies increased with increasing Sr content but Fe contents did not affect the oxygen vacancies in LSCF system. On the other hand, the substitution of Sr in BSCF systems did not cause the oxygen deficiency but the oxygen vacancies increased with decreasing the Fe contents. Experimental results of O_2-TPD in range of 500-800°C indicated that the amount of oxygen desorbed from LSCF8264 is far bigger than BSCF8264.

Department Chemistry Student's signature .
Field of study Chemistry Advisor's signature .
Academic year 2004 .

ACKNOWLEDGEMENTS

First of all, I would like to give all gratitude affectionately to my beloved parents for all their love, support and encouragement during the whole period of my study. These keep my life always going.

I am truly grateful to Dr. Oravan Sanguanruang, my advisor, for her multifarious understanding, useful guidance, kind suggestions and encouragement throughout this study. I would like to special thanks to Associate Professor Dr. Sirirat Kokpol, Associate Professor Supawan Tantayanon and Dr. Nipaka Sukpirom who act as the thesis committee.

Finally, I gratefully acknowledge the Materials Chemistry and Catalysis Research Unit (MATCAT) for Advanced Research at the Faculty of Science, Chulalongkorn University for financial support during the study, computer resources and other facilities. I also gratefully acknowledge the Energy Policy and Planning Office (EPPO), Ministry of Energy and Graduate School of Chulalongkorn University for financial support during the study.

This thesis could not have been completed without generous help of the staff members of the Material Chemistry and Catalysis Research Unit, the Organometallics Group and the Supramolecular Research Unit for their kind assistance and liberal. Special thank is forwarded to my best friends and my girlfriend for their love, understanding, encouragement, and assistance. Without them, the author would have never been able to achieve this goal.

CONTENTS

Pages

ABSTRACT IN THAI………………………………………………………... iv

ABSTRACT IN ENGLISH…………………………………………………... v

ACKNOWLEDGEMENTS…………………………………………………….. vi

CONTENTS……………………………………………………………….... vii

LIST OF FIGURES………………………………………………………….... xi

LIST OF TABLES……………………………………………………………. xiv

LIST OF ABBREVIATIONS…………………………………………….... xvi

CHAPTER I **INTRODUCTION**……………………………………. 1

CHAPTER II **THEORY**……………………………………………… 6

2.1 Structure of perovskite…………………………………. 6

2.1.1 Crystal structure……………………………….... 6

2.1.2 Tolerance factors in perovskites ………………. 7

2.1.3 Nonstoichiometry in perovskites ……………… 8

2.2 Physical properties …………………………………… 9

2.2.1 Magnetic properties…………………………… 10

2.2.2 Electrical properties……………………………. 11

2.2.3 Mixed ionic-electronic conductors…………….. 12

2.3 Oxygen adsorption property…………………………… 12

2.4 Perovskite synthesis……………………………………. 13

2.4.1 Wet chemical synthesis………………………... 13

2.4.2 Solid-state reaction..……………….………….… 14

2.4.3 Gas phase reaction…………………………….... 14

2.5 Perovskite membrane preparation by solution reaction... 15

2.5.1 Solution reaction synthesis of perovskites……... 15

2.5.2 Powder sizing…………………………….......... 20

2.5.3 Powder compacting by uniaxial pressing……… 21

Pages

2.5.4 Sintering …………………………………….. 21

2.6 Dense perovskite membranes for oxygen separation …. 23

CHAPTER III EXPERIMENTAL…………………………………… 26

3.1 Chemicals…………..……………………………..….. 26

3.2 Synthesis of perovskite powder by citrate method…...... 27

3.3 Synthesis of perovskite powder by modified citrate method……………………………………………….. 27

3.4 Perovskite membrane preparation.…………………….. 28

3.5 Calcination and sintering of the perovskite oxides...…... 29

3.6 Characterization of the perovskite oxides……………… 30

3.6.1 X-ray diffractrometry (XRD)..………….……….. 30

3.6.2 Scanning electron microscopy (SEM)…………. 30

3.6.3 Density………………………………………. 31

3.6.4 Thermogravimetric analysis (TGA)…………… 31

3.6.5 Temperature-programmed desorption (TPD)...... 31

CHAPTER IV RESULTS AND DISCUSSIONS…...……………….... 32

4.1 Perovskite powder …………………………………….. 32

4.1.1 Synthesis of LSCF perovskite powder by citrate method………………………………….. 32

4.1.2 Synthesis of BSCF perovskite powder by modified citrate method……………………….... 33

4.2. Effect of sinthering themperature to the formation of LSCF and BSCF……………………………………… 35

4.2.1 Effect of sintering on the LSCF phase transformation…………………………….……. 35

4.2.2 Effect of sintering on the BSCF phase transformation…………………………….…. 37

4.3 The Influence of A-site and B-site cations on the formation of perovskite oxides………………………… 38

Pages

4.3.1 Effect of composition to the formation of LSCF-based perovskite………………………… 39

4.3.1.1 The variation of Sr contents in $La_{1-x}Sr_xCo_{0.6}Fe_{0.4}O_{3-\delta}$ (x = 0.2, 0.3, 0.4, 0.5)…………………………………….. 39

4.3.1.2 The variation of Fe contents in $La_{0.8}Sr_{0.2}Co_{1-y}Fe_yO_{3-\delta}$ (y = 0.1, 0.2, 0.3, 0.4, 0.5)……………………………….. 41

4.3.2 Effect of composition to the formation of BSCF-based perovskite……………….……….. 43

4.3.2.1 The variation of Sr contents in $Ba_{1-x}Sr_xCo_{0.6}Fe_{0.4}O_{3-\delta}$ (x = 0.2, 0.3, 0.4, 0.5)…………………………………….. 43

4.3.2.2 The variation of Fe contents in $Ba_{0.8}Sr_{0.2}Co_{1-y}Fe_yO_{3-\delta}$ (y = 0.1, 0.2 0.3, 0.4, 0.5)……………………………. 44

4.4 Effect of composition on the morphology of perovskite membrane…………………………………………… 46

4.4.1 Effect of Sr-contents on the morphologies of LSCF perovskite membranes…..………………. 46

4.4.2 Effect of Fe-contents on the morphologies of LSCF perovskite membranes………………….. 48

4.4.3 Effect of Sr-contents on the morphologies of BSCF perovskite membranes……………..…… 49

4.4.4 Effect of Fe-contents on the morphologies of BSCF perovskite membranes……..………….. 50

4.5 Thermal Analysis..…………………………………….. 52

4.5.1 $La_{1-x}Sr_xCo_{0.6}Fe_{0.4}O_{3-\delta}$ compositions with x = 0.2-0.5…………………………………….. 52

Pages

4.5.2 $La_{0.8}Sr_{0.2}Co_{1-y}Fe_yO_{3-\delta}$ compositions with $y = 0.1$-0.5………………………………………… 54

4.5.3 $Ba_{1-x}Sr_xCo_{0.6}Fe_{0.4}O_{3-\delta}$ compositions with $x = 0.2$-0.5……………………………...………. 55

4.5.4 $Ba_{0.8}Sr_{0.2}Co_{1-y}Fe_yO_{3-\delta}$ compositions with $y = 0.1$-0.5………………………………………… 56

4.6 Oxygen temperature-programmed desorption (TPD) …. 58

CHAVTER V **CONCLUSIONS**……………………………………… 60

REFERENCES…………………………………………………………….. 62

APPENDIX………………………………………………………………. 67

APPENDIX A Telorance number……………………... 68

APPENDIX B The calculation of the oxygen deficiency at room temperature……………………. 69

VITAE……….…………………………………………………………… 70

LIST OF FIGURES

Pages

Figure 2.1 ABO_3 ideal perovskite structure showing oxygen octahedron containing the B ion linked through corners to form a three-dimensional cubic lattice………………………………………… 7

Figure 2.2 The relationship of ionic radii in perovskite structure………….. 7

Figure 2.3 Mechanism of sintering; X is the internal radius of the neck; r is the particle radius……………………………………………….. 23

Figure 2.4 Oxygen transport through a perovskite type membrane………... 24

Figure 3.1 The condition used for the calcination and sintering of LSCF…...……………………………………………………… 29

Figure 3.2 The condition used for the calcination and sintering of BSCF...……..…………………………………………………... 30

Figure 4.1 XRD patterns of (a) LSCF7364 perovskite powder after calcined at 800°C for 4 hours and (b) LSCF7364 membrane after sintered at 1,300°C for 10 hours ……………….………… 36

Figure 4.2 XRD patterns of (a) BSCF8264 perovskite powder after calcined at 1,000°C for 5 hours and (b) BSCF8264 membrane after sintered at 1,100°C for 5 hours …………………………... 38

Figure 4.3 XRD patterns of LSCF5564, LSCF6464, LSCF7364 and LSCF8264 perovskite powder after calcined at 800°C for 4 hours……………………………………………………….…. 39

Figure 4.4 XRD patterns of LSCF5564, LSCF6464, LSCF7364 and LSCF8264 perovskite membranes after sintering at 1,300 °C for 10 hours……………………………………………………… 40

Figure 4.5 Partial XRD patterns of LSCF membranes various Sr contents... 40

LIST OF FIGURES (cont.)

Pages

Figure 4.6 XRD patterns of LSCF8291, LSCF8282, LSCF8273, LSCF8264 and LSCF8255 perovskite powders after calcined at 800°C for 4 hours………..……………..…………………….... 41

Figure 4.7 Partial XRD patterns of LSCF membranes various Fe contents…..………………………………………………… 42

Figure 4.8 XRD patterns of BSCF5564, BSCF6464, BSCF7364 and BSCF8264 perovskite powders after calcined at 1,000°C for 5 hours……………………………………………………………… 43

Figure 4.9 XRD patterns of BSCF5564, BSCF6464, BSCF7364 and BSCF8264 perovskite membranes after sintering at 1,100°C for 5 hours ………………………………………………………..… 44

Figure 4.10 XRD patterns of BSCF8255, BSCF8264, BSCF8273, BSCF8282 and BSCF8291 perovskite powders after calcined at 1,000°C for 5 hours………………….…………………………….. 45

Figure 4.11 XRD patterns of BSCF8255, BSCF8264, BSCF8273, BSCF8282 and BSCF8291 perovskite membranes after sintering at 1,100°C for 5 hours………...……………………..… 45

Figure 4.12 SEM pictures of cross section of LSCF5564, LSCF6464, LSCF7364 and LSCF8264 samples sintered at 1,300°C for 10 hours……………………………………………………………….. 47

Figure 4.13 SEM pictures of cross section of LSCF8291, LSCF8282, LSCF 8273, LSCF8264 and LSCF8255 samples sintered at 1,300°C for 10 hours………………………………………………………... 48

Figure 4.14 SEM pictures of cross section of BSCF8264, BSCF7364, BSCF6464 and BSCF5564 membranes sintered at 1,100°C for 10 hours…..………………………………………………… 50

LIST OF FIGURES (cont.)

Pages

Figure 4.15 SEM pictures of cross section of BSCF8255, BSCF8264, BSCF8273, BSCF8282 and BSCF8291 membranes sintered at 1,100°C for 5 hours... 51

Figure 4.16 Relative weight loss of $La_{1-x}Sr_xCo_{0.6}Fe_{0.4}O_{3-\delta}$ as function of temperatures and Sr contents under N_2............................... 53

Figure 4.17 Relative weight loss of $La_{0.8}Sr_{0.2}Co_{1-y}Fe_yO_{3-\delta}$ as function of temperatures and Fe contents under N_2.............................. 54

Figure 4.18 Relative weight loss of $Ba_{1-x}Sr_xCo_{0.6}Fe_{0.4}O_{3-\delta}$ as function of temperatures and Sr contents under N_2. 55

Figure 4.19 Relative weight loss of $Ba_{1-x}Sr_xCo_{0.6}Fe_{0.4}O_{3-\delta}$ as function of temperatures and Fe contents under N_2.............................. 57

Figure 4.20 O_2-TPD patterns of LSCF8264 and BSCF8264..................... 58

LIST OF TABLES

Pages

Table 1.1 Applications of perovskites in materials ………………………….……….. 2

Table 1.2 Comparison of oxygen permeation properties of $La_xA_{1-x}Co_yFe_{1-y}O_{3-\delta}$ (A = Sr, Ba, Ca; x= 0.2, 0.4, 0.6; y = 0.8, 0.6, 0.4) reported in literatures………..……………………….... 4

Table 3.1 Reagents for synthesis of perovskite………………….....……….. 26

Table 4.1 List of the experimental conditions for synthesis of the LSCF (x = 0.2-0.5, y = 0.4) perovskite compounds …………………… 33

Table 4.2 List of the experimental conditions for synthesis of the LSCF (x = 0.2, y = 0.1-0.5) perovskite compounds …………………… 33

Table 4.3 List of the experimental conditions for synthesis of the BSCF (x = 0.2-0.5, y = 0.4) perovskite compounds…………………… 34

Table 4.4 List of the experimental conditions for synthesis of the BSCF (x = 0.2, y = 0.1-0.5) perovskite compounds …………………… 35

Table 4.5 XRD analyses of calcined powder and the sintered membranes of LSCF (at 25°C)…………………………………………….. 37

Table 4.6 XRD analyses of calcined powder and the sintered membranes of BSCF (at 25°C)…………………………………………….. 38

Table 4.7 Crystallographic data for LSCF perovskite various Sr contents… 41

Table 4.8 Crystallographic data for LSCF perovskite various Fe contents… 42

Table 4.9 Crystallographic data for BSCF perovskite various Sr contents… 44

Table 4.10 Crystallographic data for BSCF perovskite various Fe contents... 46

Table 4.11 Density of $La_{1-x}Sr_xCo_{0.6}Fe_{0.4}O_{3-\delta}$ membranes when x = 0.2, 0.3, 0.4 and 0.5…………………………………………………….. 47

Table 4.12 Density of $La_{0.8}Sr_{0.2}Co_{1-y}Fe_yO_{3-\delta}$ membranes when y = 0.1, 0.2, 0.3, 0.4 and 0.5 ………………………………………………….. 49

Table 4.13 Density of $Ba_{1-x}Sr_xCo_{0.6}Fe_{0.4}O_{3-\delta}$ membranes when x = 0.2, 0.3, 0.4 and 0.5…………………………………………………….. 50

LIST OF TABLES (cont.)

Pages

Table 4.14 Density of $Ba_{0.8}Sr_{0.2}Co_{1-y}Fe_yO_{3-\delta}$ membranes when y = 0.1, 0.2, 0.3, 0.4 and 0.5 ………………………………………………….. 52

Table 4.15 Oxygen non-stoichiometry (δ) in $La_{1-x}Sr_xCo_{0.6}Fe_{0.4}O_{3-\delta}$ for x = 0.2-0.5 at room temperature and 900°C under N_2…………… 53

Table 4.16 Oxygen non-stoichiometry (δ) in $La_{0.8}Sr_{0.2}Co_{1-y}Fe_yO_{3-\delta}$ for y = 0.1-0.5 at room temperature and 900°C under N_2…………… 55

Table 4.17 Oxygen non-stoichiometry in $Ba_{1-x}Sr_xCo_{0.6}Fe_{0.4}O_{3-\delta}$ for x = 0.2-0.5 at room temperature and 900°C under N_2……..…….. 56

Table 4.18 Oxygen non-stoichiometry (δ) in $Ba_{0.8}Sr_{0.2}Co_{1-y}Fe_yO_{3-\delta}$ for y = 0.1-0.5 at room temperature and 900°C under N_2…………… 57

Table 5.1 The highest dense perovskite membranes in each composition…. 61

LIST OF ABBREVIATIONS

LSCF	$La_{1-x}Sr_xCo_{1-y}Fe_yO_{3-\delta}$
°C	Degree celsius
MIEC	Mixed ionic-electronic conductivity
BSCF	$Ba_{1-x}Sr_xCo_{1-y}Fe_yO_{3-\delta}$
SOFC	Solid oxide fuel cells
a	Cubic unit lattice parameter
r	Ionic radius
t	Tolerance factor
σ_{tot}	Overall electrical conductivity
σ_e	Electrical conductivity
σ_i	Ionic conductivity
σ_{ij}	Partial ionic conductivity
Ln	Lanthanide
T_c	Calcinations temperature
TPD	Temperature-programmed desorption
EDTA	Ethylenediaminetetraacetic acid
µm	Micrometer
MAL	Malic acid
ODH	Oxalyl dihydrazine
TFTA	Tetraformal trisazine
k	Temperature constant
n, m	Mechanism growth constant
X	Internal radius of the neck
$V_{\ddot{O}}$	Oxygen vacancy
O^x_o	Lattice oxygen
h	Electron hole
P'_{O2}	Partial pressure of oxygen at higher pressure
P''_{O2}	Partial pressure of oxygen at lower pressure

LIST OF ABBREVIATIONS (cont.)

Å	Angstrom
δ	Oxygen non-stoichiometry at room temperature
δ'	Oxygen non-stoichiometry at 900°C
D_v, k_r, k_f	Functions of temperature
ml	Milliliter
XRD	X-ray diffractrometry
SEM	Scanning electron microscopy
TGA	Thermogravimetric analysis
TCD	Thermal conductivity detector

CHAPTER I

INTRODUCTION

Mixed ionic electronic conductors exhibiting both electronic and ionic conductivities have a wide range of applications such as fuel cells [1], oxygen sensors and oxygen seperating membranes [2,3] The oxygen sensors are essential for combustion control and fuel cells are expected to be a new and clean electric power source, in particular, for electric vehicles [4]. The oxygen separating membranes are used to be a potable and economical oxygen source for catalytic oxidative process. So far, tetravalent oxides with fluorite structures such as ZrO_2 and CeO_2 are widely utilized as the oxide ion conductor in various applications [4].

Since Teraoka et al. [5] reported that $La_{1-x}Sr_xCo_{1-y}Fe_yO_{3-\delta}$ (LSCF) perovskite oxide has higher ionic conductivity than fluorite structure oxides such as doped CeO_2 or ZrO_2, much attention has been paid to ABO_3 perovskite-type ionic conductors. In ABO_3 perovskite structure, where A is the larger cation in a twelvefold coordination, and B is the smaller cation in a sixfold coordination with oxygen ions. When the B ions can take a mixed-valence state, such as transition metals, the partial substitution of A site cations by other metal cations with lower valencies usually causes the formation of oxygen vacancies and a change in the valence state of the B ions in order to maintain the charge neutrality. The concentration of oxygen vacancies can also be increased by substituting ions of similar size but lower valence at the B site, for example, $A_xA'_{1-x}B_yB'_{1-y}O_{3-\delta}$ (A = La, Ba; A' = Sr, Ca; B = Cr, Fe, Co; B' = Ni, Cu). As a result, perovskite oxide shows substantial electronic conductivity as well as ionic conductivity at intermediated temperatures (600-800°C) [6], a phenomenon refered to as mixed ionic–electronic conductivity (MIEC).

In addition to the diversity of compositions mentioned above, perovskite materials can tolerance significant partial substitution and non-stoichiometry while still maintaining the perovskite structure. For example, metal ions having different valences can replace both A and B ions. This may generate a non-integral number of oxygen atoms. These flexible compositions can be represented by the related family of layered grossly oxygen deficient perovskite such as $La_{1-x}Sr_xCo_{1-y}Fe_yO_{3-\delta}$ (LSCF) [3, 7] and $Ba_{1-x}Sr_xCo_{1-y}Fe_yO_{3-\delta}$ (BSCF) [8, 9].

Because of their varied structure and composition, perovskite materials have attracted interest in various applied and fundamental in structure, physical properties and catalysis. A partial list of their potential applications is presented in Table 1.1 [10]

Table 1.1 Applications of perovskites in materials

Applications of perovskites	Materials
Photocatalyst	$SrTiO_3$
Multilayer capacitor	$BaTiO_3$
Piezoelectric transducer	$Pb(Zr, Ti)O_3$
Electrooptical modulator	$(Pb, La)(Zr, Ti)O_3$
Switch	$LiNbO_3$
Dielectric resonator	$BaZrO_3$
Thick film resistor	$BaRuO_3$
Electrostrictive actuator	$Pb(Mg, Nb)O_3$
Superconductor	$Ba(Pb, Bi)O_3$
Magnetic bubble memory	$GdFeO_3$
Laser Host	$YAlO_3$
Ferromagnet	$(Ca, La) MnO_3$
Refractory Electrode	$LaCoO_3$
Second harmonic generator	$KnbO_3$
Membrane reactor for partial oxidation	$(La, Sr) (Co, Fe)O_3$

There has been growing interest in utilizing perovskite-type LSCF for electrochemical applications. Among the various studies on LSCF compositions, Matsumoto et al. [11] found that $La_{0.2}Sr_{0.8}Co_{0.8}Fe_{0.2}O_{3-\delta}$ has the highest catalytic activity as an electrode for oxygen evolution in alkaline solution. Teraoka et al. have investigated the oxygen adsorption [12] and the oxygen permeation properties [12, 13] of LSCF. Their findings confirmed that perovskite-type ABO_3 compositions containing more than two types of transition metal ions on the B site are always more reactive (for oxygen reduction) than those with only one type of transition metal ion. They also concluded that LSCF compositions with higher Sr and Co contents have higher oxygen permeability, which can exceed by more than one order of magnitude that of stabilized zirconia. This occurs because Sr on the A-site lattice of LSCF acts as an acceptor, enhancing the formation of oxygen vacancies. In addition, Co ions on the B site appear to have a smaller binding energy for oxygen than do Fe ions. Therefore, the degree of oxygen deficiency is expected to be higher in those LSCF compositions with a higher Co content. The use of these compounds as a catalyst for the combustion of hydrocarbons, as well as for the reduction of hydrogen peroxide in alkaline solutions, has also been studied by Zhang et al. [14].

Many researchers investigated the suitable perovskites materials with the best combination of oxygen permeability and stability. Teraoka et al. mentioned [12] that LSCF based perovskite-type ceramic membranes have considerably high oxygen permeation fluxes at high temperatures. It was found that the oxygen flux tended to increase with the increase of the substitution of Sr^{2+} for La^{3+} and Co^{3+} for Fe^{3+}, but a small amount of Fe was necessary to preserve the perovskite type structure at high Sr contents. They [15] reported later that very high oxygen fluxes through the A-site substitution compositions, $La_{0.6}A_{0.4}Co_{0.8}Fe_{0.2}O_{3-\delta}$ (A = Sr, Ba, Ca) series oxides, which become highly defective at elevated temperatures and reduced oxygen partial pressure. The oxygen permeation flux of A-site substitution decreases in the order, Ba > Ca > Sr. Stevenson et al. [16] also have studied oxygen permeability of A-site substitution perovskite-type oxides. Their work focused on $La_{0.4}A_{0.6}Co_{0.2}Fe_{0.8}O_{3-\delta}$ (A = Sr, Ba, Ca) oxides system. They reported that the oxygen permeation fluxes decrease in the order Sr > Ba > Ca. A comparison of oxygen permeation properties of $La_xA_{1-x}Co_yFe_{1-y}O_{3-\delta}$ (A = Sr, Ba, Ca; x = 0.2, 0.4, 0.6; y = 0.8, 0.6, 0.4) reported by these researchers is shown in Table 1.2.

Table 1.2 Comparison of oxygen permeation properties of $La_xA_{1-x}Co_yFe_{1-y}O_{3-\delta}$ (A = Sr, Ba, Ca; x= 0.2, 0.4, 0.6; y = 0.8, 0.6, 0.4) reported in literatures

Studied	Powder synthesis	Membrane	Thickness (cm)	JO_2 (900 °C) ($cm^3.cm^{-2}.min^{-1}$)	E_a ($kJ. mol^{-1}$)
Teraoka (1998)	Solid-state reaction	$La_{0.6}Sr_{0.4}Co_{0.8}Fe_{0.2}O_{3-\delta}$	0.2	0.62	86.3
		$La_{0.6}Ba_{0.4}Co_{0.8}Fe_{0.2}O_{3-\delta}$	0.2	2.11	57.2
		$La_{0.6}Ca_{0.4}Co_{0.8}Fe_{0.2}O_{3-\delta}$	0.2	1.80	75
Stevenson (1996)	Glycine-nitrate combustion	$La_{0.4}Sr_{0.6}Co_{0.2}Fe_{0.8}O_{3-\delta}$	0.2	0.55	91.7
		$La_{0.4}Ba_{0.6}Co_{0.2}Fe_{0.8}O_{3-\delta}$	0.2	0.45	86.8
		$La_{0.4}Ca_{0.6}Co_{0.2}Fe_{0.8}O_{3-\delta}$	0.2	0.07	67.5
		$La_{0.2}Sr_{0.8}Co_{0.2}Fe_{0.8}O_{3-\delta}$	0.2	0.68	82.0
		$La_{0.2}Ba_{0.8}Co_{0.2}Fe_{0.8}O_{3-\delta}$	0.2	0.42	62.7

Due to the difficulties in high temperature permeation measurement, only limited research groups have conducted studied on the oxygen permeation properties of mixed-conducting ceramic membranes. Many inconsistencies are found among the limited data reported, even with the same material under similar conditions. For example, the oxygen permeation data reported by Jacobson et. al. on $SrCo_{0.8}Fe_{0.2}O_{3-\delta}$ were generally larger by at a factor of five than those mentioned by Kruidhof et. al. [16] but smaller than those exhibited by Teraoka et. al. [13] over the same temperature range. Therefore, more research is needed in order to achieve a quantitative understanding of oxygen permeation through these mixed-conducting ceramic membranes.

The oxygen permeation fluxes of the membranes made from these oxides can be influenced by many factors such as membrane material, membrane thickness, microstructure and temperature at which the membranes are to be used. And in spite of all the interest in the perovskitetype oxide, there is little published information relating the structural, thermal and oxygen permeation of these materials, particularly for compositions with low Sr and Fe contents.

Therefore, the objectives of this study are as follows: (1) to synthesize fine particles of the single-phase $La_{1-x}Sr_xCo_{1-y}Fe_yO_{3-\delta}$ (LSCF) and $Ba_{1-x}Sr_xCo_{1-y}Fe_yO_{3-\delta}$

(BSCF) (x = 0.2-0.5 and y = 0.1-0.4) by using the citrate or the modified citrate methods. (2) to study the effect of the preparation variables such as amounts of Sr and Fe in perovskite-type oxides and sintering temperatures for preparations of dense perovskite membranes. (3) to test the oxygen permeation of selected perovskite membranes.

CHAPTER II

THEORY

Perovskites are named after the mineral $CaTiO_3$ which was identified by the Russian mineralogist L.A. Perovski [17]. The perovskite materials occupy a prominent place in the materials science world because of its very favourable characteristics such as structural, ionic as well as electronic conductivity, high electrocatalytic activity and high thermodynamic stability. They are immensely used as electrode materials for solid oxide fuel cells (SOFC) [18], gas seperation membranes, catalysts for oxidations of hydrocarbons [3] and humidity sensors [19]. This study is focused on the use of mixed conducting perovskites as oxygen separation membranes. This chapter includes the general review of perovskite-type structure physical properties, synthesis methods, membrane preparation and the oxygen permeation through a perovskite membrane.

2.1 Structure of perovskites [17]

2.1.1 Crystal structure

The ideal perovskite-type structure is cubic with the generic formula of perovskite-type oxides ABO_3, where A is a larger cation and B is a smaller cation. In this structure, the B cation is six-fold coordinated and the A cation is twelve-fold coordinated with the oxygen ions. For example, in $SrTiO_3$ (ionic radius Sr^{2+} = 1.52 Å, and ionic radius Ti^{4+} = 0.745 Å), strontium would be denoted as the A cation and titanium as the B cation. Perovskite also can be regarded as ReO_3-type frame work. Figure 2.1 depicts the corner sharing octahedral that form the skeleton of the structure, in which the center position is occupied by the A cation. Alternatively, this structure can be viewed with the B cation placed in the center of the octahedron and the A cation is in the center of the cube.

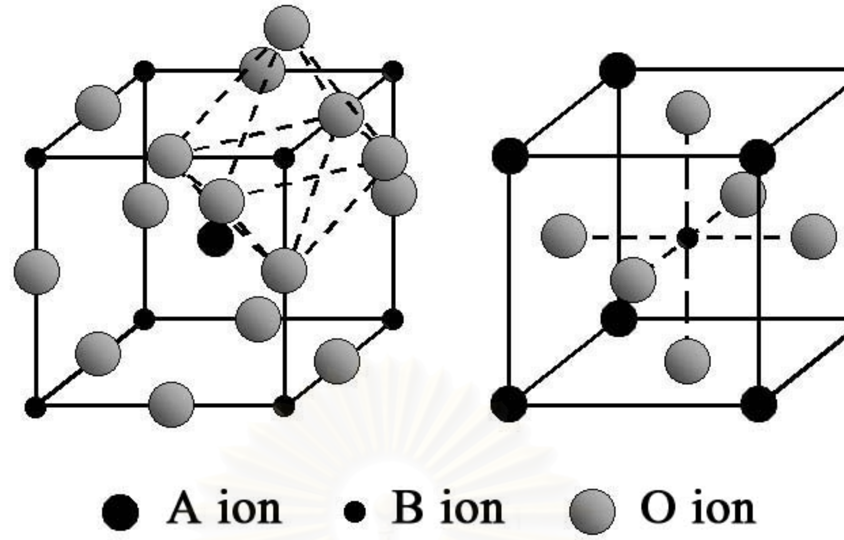

Figure 2.1 ABO_3 ideal perovskite structure showing oxygen octahedron containing the B ion linked through corners to form a three-dimensional cubic lattice.

2.1.2 Tolerance factors in perovskites

In the ideal perovskite structure, the size and coordination preferences of three or more ions need to be satisfied simulatneously by the structure; it is, however, rarely possible that all these choice can be accommodated perfectly. This can be illustrated for the perovskite structure by deriving a relationship between the radii of the various ions. Figure 2.2 shows the relationship between ionic radii in the perovskite structure.

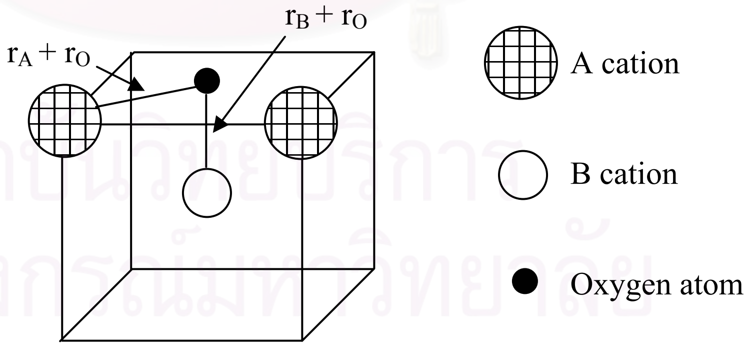

Figure 2.2 The relationship of ionic radii in perovskite structure.

$$a = 2xB - O = 2(r_B + r_O) \tag{2.1}$$

and

$$a = \frac{1}{\sqrt{2}} x 2 x A - O = \sqrt{2}(r_A + r_O) \tag{2.2}$$

hence,

$$2x(r_B + r_O) = \sqrt{2}x(r_A + r_O) \tag{2.3}$$

where the atoms are touching one another, the B-O distance is equal to $a/2$ (a is the cubic unit cell parameter) while the A-O distance is ($a/\sqrt{2}$) and the following relationship between the ionic radius (r) holds shown in Equation 2.3. In general, the perovskite structure is formed if the tolerance factor, *t*.

$$t = \frac{(r_A + r_O)}{\sqrt{2}(r_B + r_O)} \tag{2.4}$$

The ideal perovskite is the cubic structure with the tolerance factor close to 1.0 at high temperature. The perovskite structure is stable in the range $0.75 < t < 1.0$, and is cubic in the range $t > 0.95$. [8, 9] Deviations from the ideal structure are well known as orthorhombic, rhombohedral, tetragonal, monoclinic and triclinic symmetry. The distorted structure may exist at room temperature but it transforms to the cubic structure at ambient temperature. [20]

2.1.3 Nonstoichiometry in perovskites

Nonstoichiometry in perovskites can arise from cation deficiency (in the A or B site), anion deficiency, or anion excess. For the cation deficiency, A-site cations can be missing without collapse of the perovskite network because of the stability of the BO_3 group [20]. On the contrary, B-site vacancies are not energetically favored because of the large formal charge and the small size of the B cations in perovskites. Nevertheless, an oxygen vacancy in perovskites is more common than a cation deficiency.

Many oxygen-deficient perovskites can be described on the basis of complex perovskite-related super-structures of general formula $A_nB_nO_{3n-1}$, in which the stacking manner depends on the size, electronic configurations, and coordination numbers of A and B cations. Oxygen vacancies are accomplished by substituting ions of similar size but different valence. For example, some of the La^{3+} ions in $LaBO_3$ are replaced by Sr^{2+} to form $La_{1-x}Sr_xBO_{3-\delta}$, and therefore, oxygen vacancies are formed.

The former composition can be considered as an anion-deficient perovskite with one-sixth of the oxygen ions being vacant. Oxygen vacancies are ordered in alternate [001] BO_2 planes of the cubic structure such that alternate [110] rows of oxide anions are missing.

2.2 Physical properties [21]

The perovskite structure class is one of the most commonly occurring and important in all of materials science. Physical properties of interest among perovskites include superconductivity, colossal magnetoresistance, ionic conductivity, and a multitude of dielectric properties, which are of great importance in microelectronics and telecommunication. Because of the great flexibility inherent in the perovskite structure there are many different types of distortions which can occur from the ideal structure. These include tilting of the octahedra, displacements of the cations out of the centers of their coordination polyhedra, and distortions of the octahedra driven by electronic factors (i.e. Jahn-Teller distortions). Many of the physical properties of perovskites depend crucially on the details of these distortions, particularly the electronic, magnetic and dielectric properties which are so important for many of the applications of perovskite materials.

In order to characterize the materials, it is more often to measure their electronic and ionic conductivity instead of concentrations of electrons (holes) and mobile ions (vacancies). The calculated ionic and electronic conductivity, which were separately measured by using 4-probe ionic direct current and ordinary 4-probe direct current techniques, respectively.

In all materials that there are in principle nonzero electronic and ionic conductivity, the overall electrical conductivity σ_{tot} is the sum of electronic conductivity σ_e and ionic conductivity σ_i, as Equation (2.5),

$$\sigma_{tot} = \Sigma\, \sigma_{ij} + \sigma_e \tag{2.5}$$

where σ_{ij} is the partial conductivity (in $\Omega^{-1}cm^{-1}$) of the *jth*-type ionic charge carriers presenting in the solid. Ionic charge carriers can be either atomic in nature or normally defects of either the anionic or cationic sublattice. Ionic conductivity occurs normally via interstitial sites or by hopping into a vacant site (vacancy motion) or a more complex combination based on interstitial and vacant sites.

Electronic (electron/hole) conductivity occurs via delocalized states in the conduction-valence band or via localized states by athermally assisted hopping mechanism. The presence of electronic conduction in perovskites proceeds via B.

Lattice cations through overlapping B-O-B bonds via a mechanism known as the Zerner double exchange process is shown in Equation (2.6) [21]:

$$B^{n+}\text{-}O^{2-}\text{-}B^{(n+1)} \longrightarrow B^{(n+1)+}\text{-}O^{2-}\text{-}B^{(n+1)+} \longrightarrow B^{(n+1)+}\text{-}O^{2-}\text{-}B^{n+} \qquad (2.6)$$

This process is facilited by strong overlap of the B site cation and O^{2-} orbital which is maximized for B-O-B angles at 180 °C, i.e., cubic structure. In the orthorombic structure, the tilting of BO_6 give rise to a decrease in the B-O-B overlap and thus would be expected to provide a larger barrier to electronic conduction. In the above double exchange mechanism, electronic conduction requires the presence of B site cations with multiple valences. Furthermore, the electronic conduction can be n-type or p-type, depending on the material properties and ambient oxygen partial pressure. The energy level shifts from the center of the energy gap toward the empty zone for an n-type semiconductor or the filled band for a p-type semiconductor. An n-type conductor is an electron conductor while a p-type conductor is an electron hole conductor. It was noticed that perovskites with high p-type electronic conductivity tended to be active for deep methane oxidation reactions while those with high n-type electronic conductivity, ionic conductors, and insulators were all found to be more selective to C_2 compounds [22].

2.2.1 Magnetic properties

In the ideal cubic perovskite structure, each atom of oxygen is shared by two B^{3+} ions, forming a B-O-B angle of 180°. Such a configuration is favorable for super exchange interactions between magnetic B^{3+} cations. This exchange usually results in anti-parallel coupling of nearest-neighbor magnetic moments. When the B^{3+} ions are in two sub lattices ($A_2BB'O_6$) the other spin arrangements are possible. If B′. is a diamagnetic ion, the B^{3+} ions are aligned anti-ferromagnetic, and the most important exchange mechanism is believed to be a longer range super exchange interaction through two oxygens of the type B-O-B′-O-B. The B-B separation is now considerably longer than the 0.4 nm separation found in the ideal perovskite. The $LnFeO_3$ (Ln = lanthanide) perovskites are those that have attracted the most attention because of their possible applications as technological magnetic materials [23]. These compounds show a weak spontaneous magnetic moment, which is attributed to a slight canting of the iron moments, which are otherwise anti-ferromagnetic aligned. Similarly, $LnMnO_3$ shows very interesting magnetic properties. These manganites containing mostly Mn^{3+} or Mn^{4+} ions show anti-ferromagnetic behavior. However, ferromagnetic behavior is observed in the range from 25 to 35% Mn^{4+}. A weak magnetic interaction was found between Mn^{3+} ions, together with a negative interaction between Mn^{4+} ions and a strong positive interaction between Mn^{3+} and Mn^{4+}. A similar kind of behavior was found for the combination of Co^{3+} and Co^{4+}, but the Cr and Fe compounds were found to be anti-ferromagnetic.

2.2.2 Electrical properties

The electrical conductivity of perovskites also shows wide variations. Several compounds have been used for their dielectric properties, while others show metallic conductivity, although most are semiconductors. As for other compounds, the electrical behavior in perovskites depends on the outermost electrons, which may be localized at specific atomic sites or may be collective. Since localized electrons may carry a spontaneous moment, there is a strong correlation between the electrical and magnetic properties of perovskites. Rare-earth perovskites containing transition ions show widely differing electrical properties. The electrical properties of perovskites have aroused special interest since the discovery in 1986 of superconductivity at 40 K in cuprates. These cuprates are whole superconductors, exhibiting a mixed valence of copper Cu^{2+}-Cu^{3+}. Among these, the exception is Ce-doped Nd_2CuO_4, with T_c close to 25 K, which belongs to a different structural type and is an electron superconductor. All these compounds have a common feature, the two-dimensional character of the structure, which has been shown to be an important factor for the existence of superconductivity at high temperature [20].

2.2.3 Mixed ionic-electronic conductors

It exhibits both ionic and electronic conductivity for example $La_{1-x}Sr_xBO_{3-\delta}$. When the B ions can take a mixed-valence state, charge neutrality is maintained by both the formations of oxygen vacancies and a change in the valence state of the B ions. The oxides may show both high oxygen ion conductivity due to the high oxygen vacancy concentration, and a high electronic conductivity due to the mixed-valence state [24]. The concentration of oxygen vacancies can also be increased by mild B-site ion substitution, such as Cu and Ni ions, which naturally take the divalent oxidation state [15]. If the valence state of the B ions is fixed, neutrality is maintained only by the formation of oxygen vacancies. The oxides may be predominantly ionic conductors, in this case.

2.3 Oxygen adsorption property

Oxygen adsorption on perovskite oxides has been studied mainly because of these compounds as redox catalysts. They were used for redox reactions in connection with purification of automobile exhaust gases [25]. Thus the study by temperature-programmed desorption (TPD) of oxygen adsorption on perovskite oxides has attracted considerable interest.

Yamazoe et al. [26] reported the first oxygen TPD results from perovskites. The objective was to study the influence of partial substitution of La^{3+} by Sr^{2+} in $La_{1-x}Sr_xCoO_3$ oxides on their surface and catalytic properties. Oxygen TPD peaks from perovskites appeared two oxygen desorption peaks after adsorption on $La_{1-x}Sr_xCoO_3$ at 1023 K. The low-temperature peak (α-type) was attributed to adsorbed oxygen, whereas the high- temperature peak (β-type) was ascribed to lattice oxygen. They concluded that the amount of desorbed oxygen from $La_{1-x}Sr_xCoO_3$ increased with increasing x-substitution. Since A-site substitution with a divalent ion is known to induce the formation of oxygen vacancies.

In a recent contribution, Yokoi and Uchida [27] observed that the amount of O_2 desorbed and the temperature of the α-type oxygen desorption from $LaMO_3$ (M = Cr, Mn, Fe, Co, Ni) tended to decreased with the increasing atomic number of the transition metal. The β-type oxygen desorption peak was found to be more specially associated with the M cation, although it is also affected by La-site substitution.

2.4 Perovskite synthesis

Perovskite synthesis plays a critical role in determining the particle size of perovskite powder, and consequently has an influence on the microstructure of perovskite membrane. Cui and Lui [28] reported in their study that pervovskites synthesized by different methods had different temperature of crystal transformation and the surface defect of powders dried by a supercritical method improved the formation of the crystal structure. Zhang et al. [29] reported that the grain size had a strong effect on the oxygen permeation flux for $SrCo_{0.8}Fe_{0.2}O_{3-\delta}$ membrane. But Qi et. al. [30] thought that the deviation of composition from the desired stoichiometry, which resulted from the different synthesis methods, was the major reason for the discordant of oxygen permeation data.

There are many routes to synthesize perovskite, such as a conventional solid-state reaction method and a wet chemical process that includes thermal decomposition of cyanide, metal-EDTA, chemical coprecipitation and the sol-gel process etc.

2.4.1 Wet chemical synthesis

Wet chemical process is a traditional way for making perovskite materials usually adopt mixing the constituent oxides, hydroxides and carbonates. Since this method produces a large particle size material, this approach frequently requires repeated mixing and extended heating at high temperature to generate a homogeneous and single-phase material. In order to overcome the disadvantages of low surface area and limited control of the micro-structure inherent in the high temperature process, precursors generated by sol-gel preparations or coprecipitation of metal ions by precipitating agents such as hydroxide, cyanide, oxalate, carbonate, citrate ions etc., have been used.

These gel or coprecipitated precursors can offer molecular or near molecular mixing and provide a reactive environment during the course of subsequent heating and decomposition. Because of the improved solid-state diffusion resulting from the improved mixing, they need a relatively lower temperature to produce similar materials compared to the traditional methods. These methods frequently offer additional advantages, such as atomic/molecular level homogenous mixing of constituent metal ions, better reactivity at lower reaction temperatures, high purity, and good control of stoichiometry and high sinter ability.

A convenient way of classifying the methods, which state from solution, is to consider the means used for solvent removal. Two basic classes exist. The first is based upon precipitation with subsequent filtration, centrifugation, etc., used to separate the solid and liquid phases. The second basic method depends upon thermal processes, e.g., evaporation, sublimation, combustion, etc., to remove the solvent. The latter method is preferred because of the possible contemporaneous conversion of the residue into the desired product.

A more subtle concern is the choice of the presumably inert anions, which will be determined by the pH values, ionic strength, degree of super saturation and impurities. This is important firstly because of the tendency of these ions to become incorporated in the final product and secondly because there are subsequent effects can vary dramatically. Conditions that favor large particle size, slow growth and equilibrium will generally produce the purest precipitate.

2.4.2 Solid-state reaction

The most common procedure for perovskite oxides synthesis via solid state reactions is the calcination of a homogenous mixture of the corresponding oxides and carbonates or nitrates. This method is very convenient but the impurities are introduced from raw materials, milling media, and the calcination container. Because of the high temperature required for the complete reaction. The problems such as multiphase have to be minimized in order to generate homogeneous high performance perovskite.

2.4.3 Gas phase reaction

The deposition of perovskite films with a specific thickness and composition generally requires gas phase reaction or transport. Many physical techniques have been developed for gas phase deposition such laser ablation, molecular beam epitaxy, dc sputtering, magnetron sputtering, electron beam evaporation and thermal evaporation. In general, they can be divided into two categories based on the target they use. The first type uses separate targets where a different speed of deposition for each element has to be determined. The second method uses the performed perovskite material itself as target and the stoichiometric phase is transported to the substrate by sputtering or ablation techniques. Gas depositions can be divided further into three categories: (1) deposition at low substrate temperature followed by a post-annealing at elevated temperatures, (2) deposition at intermediate temperature of 873 to 1073 K, and (3) deposition at crystallization temperature under an appropriate atmosphere.

2.5 Perovskite membrane preparation by solution reaction

2.5.1 Solution reaction synthesis of perovskites

According to the perovskite synthesis via solid-state reaction has found that the impurities occurred. For this reason, the improvement of the perovskite synthesis has been interested continuously.

It is widely known that the synthesis of ceramic powders by using the conventional solid-state synthesis promotes the crystal growth and resulting in a hard agglomeration. The good sintered ability may be obtained when the preparation procedure is weak agglomerates are formed. Therefore, the properties of the raw material powder are largely determined by the properties of the raw material powders, which several requirements are imposed, fine particles (< 1 μm), narrow size range, no aggregation, controlled particle shape, uniformity in chemical and phase compositions, and high purity. [31]

Solution reactions have been developed from solid-state synthesis to produce the required properties of raw perovskite powders, such as spray-pyrolysis, freeze drying [32], precipitation [33], sol-gel [34] and liquid mix process, etc.

Liquid mix process is a generic name for various processes that start with a homogeneous solution containing the desired cations, which use additives and evaporation to convert the homogeneous liquid to rigid cross-linked polymer, and which utilize heat to convert the polymer into a homogeneous oxide powder. The initial process was pioneered by Pechini and is referred to either as Pechini process [35]. The following steps are used to achieve a powder.

1. An aqueous solution is prepared with metal alkoxides, oxides, hydrated oxides, or carbonates in an alpha-hydroxycarboxylic acid such as citric acid; the ratio of metal ions can be precisely controlled.
2. A polyhydroxy alcohol such as ethylene glycol is added and the liquid is heated to 150 to 250°C to allow the chelates to undergo polyesterification.
3. Heating is continued to remove excess water, resulting in solid polymeric resin.
4. The temperature is increased to about 400°C to char or decompose the resin.
5. The temperature is further increased to 500 to 900°C to form crystallites of the mixed oxide composition. The crystallites are typically 20 to 50 nm and clustered into agglomerates.

Solubility is one of the most important considerations in solution techniques. Metal oxalates, sulphates, nitrates, chlorides, and acetates were avoided. Because of the low solubility of these compounds could lead to the phase separation in the final product. Not only it is desirable that solubility being high in order to minimize the amount of solvent which must be removed, but also the particular components must be compatible, e.g., iron sulfates could not be combined with barium chloride. Because of barium sulfate would precipitate in the reaction.

A variety of modifications of the Pechini process have been developed. One was called amorphous citrate process that involves producing precursor from citric acid and metal nitrate before thermal decomposition. For example Baythoun and Sale study the production of Sr-substituted $LaMnO_3$ perovskite powder by the amorphous citrate process. The manganese citrate-nitrate precursor may be represented as in Equation 2.7 [36]:

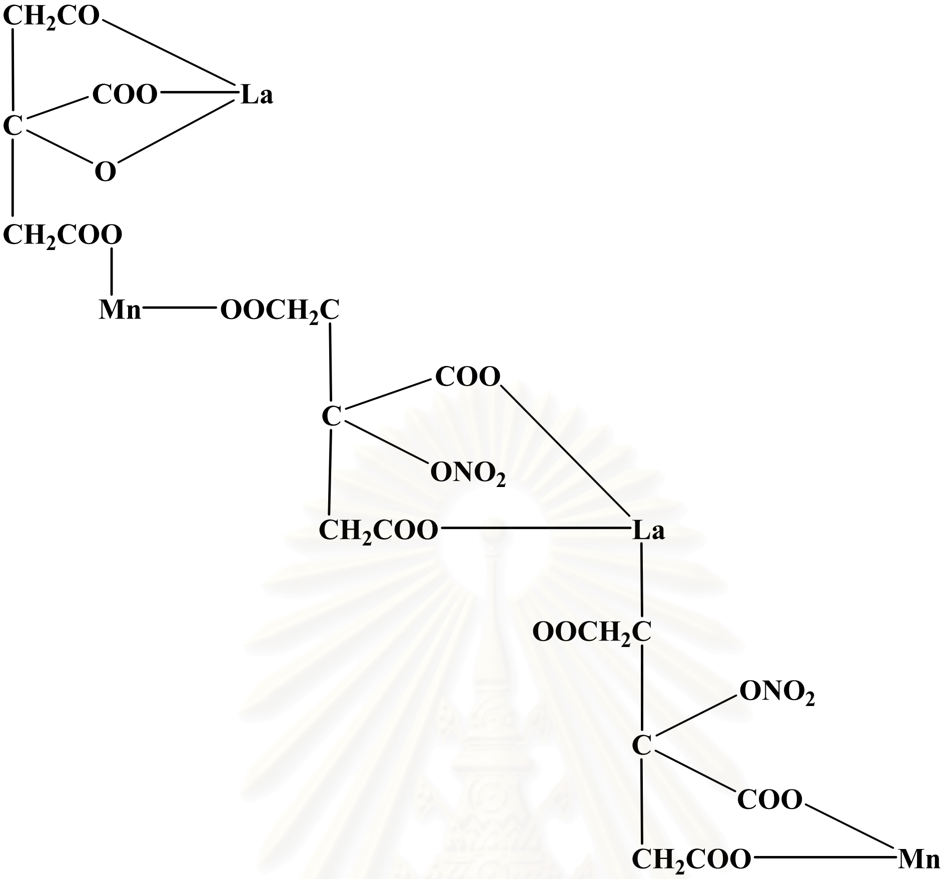
CH₂CO
COO
La
C
O
CH₂COO
Mn
OOCH₂C
COO
C
ONO₂
CH₂COO
La
OOCH₂C
ONO₂
C
COO
CH₂COO
Mn

(2.7)

In the complex the lanthanum is triply charged and replaces in one case the hydrogen of three –COOH groups (as in normal citrate formation) and in another case it replaces the hydrogen of one –OH group and two –COOH groups. Manganese in the divalent state replaces the hydrogen in two –COOH groups while NO_2 replaces the hydrogen of one –OH group.

In all cases the minimum amount of citric acid used was that necessary to bond the metals if all the NO_3^- ions were replaced. However, the amounts of metal and citric acid should not less than equimolar. If the high amount of citric acid was used, Mn_2O_3 was presented from the complex as in Equation 2.8:

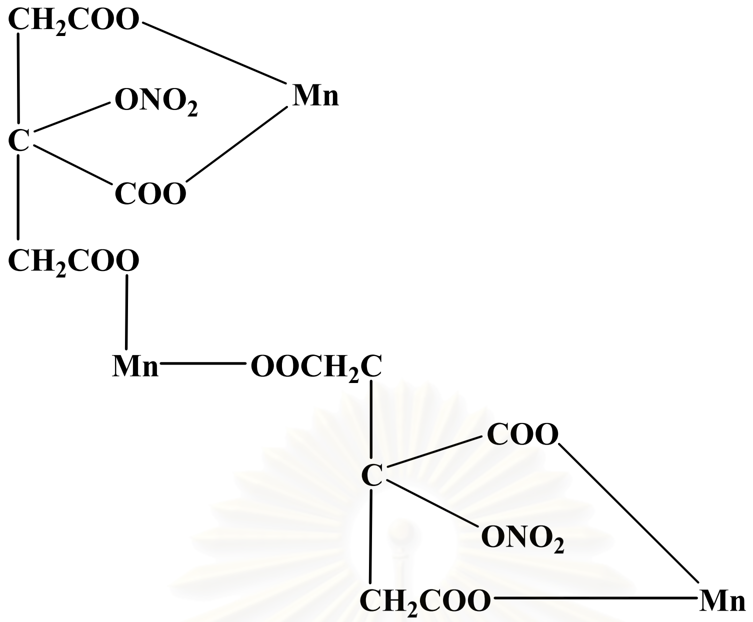

(2.8)

The formation of above structure would allow some citric acid, water, and nitrate ions to be lost during the preparation of gel. Every three molecules of citric originally present one remains uncombined and may be removed from the mixture by either evaporation or decomposition to yield acetone, carbon dioxide and water during the precursor preparation in the vacuum oven. The formation of this complex would also liberate NO_3^- groups for each two molecules of $Mn(NO_3)_2$ originally present in solution. The calcination temperature should be higher than 800°C because the wide range of homogeneity at lower temperatures was a result of the segregation of $Sr(NO_3)_2$ during precursor preparation and the production of $SrCO_3$ during precursor decomposition. However, it should not be higher than 1,100°C because these would inevitably lead to a decrease in surface area. They also reported that the best compromise would appear and initial treatment of the precursor at 700°C to yield the high surface area followed by an increase in temperature to 1,100°C for a period of up to 4 hours to remove carbon.

Other modifications of the Pechini process were called the citric acid pyrolysis method [37]. For synthesis of $YBa_2Cu_3O_{7-\delta}$, the mixed metal oxides were dissolved by nitric acid. Then pH value of the dissolved nitrate solution was adjusted by NH_4OH and then NH_4NO_3 served as fuel.

The synthesis method has been developed so far. One involves the use of metal nitrates. It is called the glycine-nitrate process, uses glycine instead of citric acid [38]. The glycine performs two functions. First, it forms complexes with metals cations and increases their solubility. This seems to prevent selective precipitation and segregation during evaporation. Second, the glycine serves as a fuel during charring. Specifically, metal nitrates are combined with glycine in water and evaporated until a homogeneous viscous liquid is formed. The liquid is further heated to about 180°C and auto-ignites. Temperatures rapidly reach 1,100^{o}C to 1,450^{o}C and nearly instantly convert the material to fine, relatively no agglomerated crystallites of the mixed oxide composition and structure. The glycine nitrate precursor liquid can also be converted to homogeneous mixed oxide powders in a conventional spray drying apparatus.

Teraoka et al. [39] synthesized $La_{0.8}Sr_{0.2}MO_3$ (M = Mn, Co) compounds by a hydroxy acid-aided process that was composed of the evaporation-to-dryness step of the mixed aqueous solution of metal nitrates and a hydroxy acid, followed by calcination in air. When citric or malic acid was used, well-crystallized perovskite-type oxides were formed at 550-600°C, which was 250-300°C lower than the temperature for the conventional nitrate process. The malic acid-aided process gave oxides with larger square surface areas than those obtained with the citric acid-aided process, and the resulting large surface area oxides show excellent catalytic performance for the combustion of methane.

The malic acid-aided (MAL) process with the adjustment of pH of starting solutions to appropriate values (3.0-3.5 for $La_{0.8}Sr_{0.2}CoO_3$ and 4.0 for $La_{0.8}Sr_{0.2}MnO_3$) was quite effective to produce high surface-area oxides at lower calcination temperatures. The effective of the pH adjustment originated from the formation of homogeneous precursors by the control of the dissociation of carboxylic acid group and the formation of metal-acid complex.

Suresh et al. [40] synthesized $La_{1-x}Sr_xFeO_3$ where x = 0.0-1.0 by the solution combustion method using corresponding metal nitrates, oxalyl dihydrazide (ODH) or tetraformal trisazine (TFTA). Theoretical equation for the formation of ferrite $(LaSr)FeO_3$ assuming complete combustion of the redox mixtures can be written as Equation 2.9:

$$(1-X)La(NO_3)_3 + XSr(NO_3)_2 + Fe(NO_3)_3 + 3(CON_2H_3)_2 \text{ ; } X = 0\text{-}1.0$$

$$\downarrow$$

$$La_{1-X}Sr_XFeO + 6CO_2\text{ (g)} + 9H_2O\text{ (g)} + 9N_2\text{ (g)} \tag{2.9}$$

(24 mols of gases /mol of $LaSrFeO_3$)

The powder densities and surface area of TFTA derived ferrites were found to be higher than those of ODH derived ferrites. The average agglomerate size distribution is narrower for ODH derived ferrites than the TFTA ferrites and the average agglomerate sizes are 0.89 μm and 4.8 μm respectively.

The perovskite powders made by wet chemical methods are very fine, and can be no agglomerated, which facilitates the densification process. The sintering temperature can be several hundred degrees Celsius lower for the powders made by wet chemical methods than for those made by conventional solid-state synthesis methods. When comparing several techniques in wet chemical methods, liquid mix process is distinguished in the case of less energy consumption, simplest technology, and potential to get fine particles and a single-phase powder. Both adding several acids such as citric, malic acid, or etc. and adjusting the pH of aqueous solution are used to provide the fine homogeneous perovskite with the high surface area.

2.5.2 Powder sizing

Powder particles are influenced on compacting and sintering. In most cases the objective of the pressing step is to achieve maximum particle packing and uniformity, so that minimum shrinkage and retained porosity will result during densification. A single particle size does not produce good packing. Optimum packing for particles all the same size results in over 30% void space. Adding particles of a size equivalent to the largest voids reduces the void pore volume to 23%. Therefore, to achieve maximum particle packing, a range of particle sizes is required.

Hard and dense agglomerates in ceramic powders usually result in large interagglomerate pores after sintering. Therefore small particle size is important because it facilitates the high strength of green disc and the sintering process. The primary driving force for densification of a compact powder at high temperature is the change in surface free energy. Very small particles have high surface areas. The high surface free energy and very strong thermodynamic driving force decrease their surface by bonding them together. The particle with approximate sizes of 1 μm or less can be compacted into a porous shape and sintered at a high temperature to near-theoretical density [41]. Typically, the finer the powder, the greater its surface area, and the lower the temperature and shorter time for densification. Long time of the sintering temperature causes of the increasing in grain growth and lowering strength.

Calcined powder is not usually available with the optimum particle size distribution. The ball milling and screening are the common techniques to achieve the desire particle size of powder.

2.5.3 Powder compacting by uniaxial pressing [41]

Uniaxial pressing is accomplished by placing the powder in to a rigid die and applying pressure along a single axial direction through a rigid plunger, or piston to achieve compacting. Pressing results in the direct contact of particles, reduces the average distance between particles, and changes the shape of particles. The apparent density of a compact was controlled by mixing of the proper various particles size fractions.

To enhance the compacting, before pressing, the powder should be disaggregated by mixing the powder with solvent such as isopropanol in the ultrasonic bath or added a couple drops of acetone to reduce the surface tension.

2.5.4 Sintering [42]

Sintering by definition is a process of permanent chemical and physical change accompanied by reduced porosity by the mechanism of grain growth and grain bonding. The driving force for sintering is the decrease in surface free energy that occurs as the surface area of the polycrystalline aggregate is reduced. This process can be achieved by solid-state reaction or alternatively in the presence of a liquid phase. When a powder aggregate is sintered, necks form between the particles, and the aggregate may increase in density. The growth of the neck is due to the transport of matter or of the counter-flow of vacancies between the particles and the pores. In crystalline powder, its transport occurs by diffusion (bulk, surface, or grain boundary diffusion), whereas in amorphous materials, it occurs by viscous flow. Kuczynski has defined the neck growth as in Equation 2.10.

$$X^{n}/r^{m} = \mathrm{kt} \qquad (2.10)$$

Where *X* and *r* are defined in Figure 2.3, *t* is the time, *k* is the temperature dependent constant, *n* and *m* are constants dependent on the mechanisms of growth, viscous or bulk diffusion, surface diffusion, or evaporation and condensation. Three stages of sintering can be distinguished. The early stage or initial stages during which the necks form at points of particle contact and the particles usually center approach each other. At this stage the individual particles are still distinguishable. The intermediate stage during that the necks become large, resulting in the formation of an interconnected pore structure. The third or the final stages during, the pores become isolated. Elimination of the interconnectivity of pores eliminates surface and vapor transport.

Closed pores isolated from grain boundaries shrink very slowly because grain boundary diffusion is far away from the pores. The growth of grains, therefore, hinders the attainment of theoretical density, since the pore's growth is also enhanced. It is essential, therefore, to retard grain growth so that densification of the compact can continue to the theoretical limit. This is particularly important with the present trend of using ultrafine particles as starting materials for the fabrication of technical ceramics. Surface diffusion becomes important in the case of very fine particles. Grain boundary diffusion and volume diffusion are the main mechanisms causing shrinkage of the neck, whereas surface diffusion does not contribute to any shrinkage. The most important diffusion paths during the sintering of two spheres with a grain boundary are surface diffusion, grain boundary diffusion, volume diffusion from the grain boundary to the neck surface, and volume diffusion from the sphere surface to the neck surface. The sintering rate also affected by the crystallization and growth processes, which occur concurrently. The sintering rate is reduced when there is intensive grain growth because when diffusion forms the pores occurs toward the boundaries of individual grains, the distance over which diffusion occurs with a reduction in pores is determined by the size of the crystals.

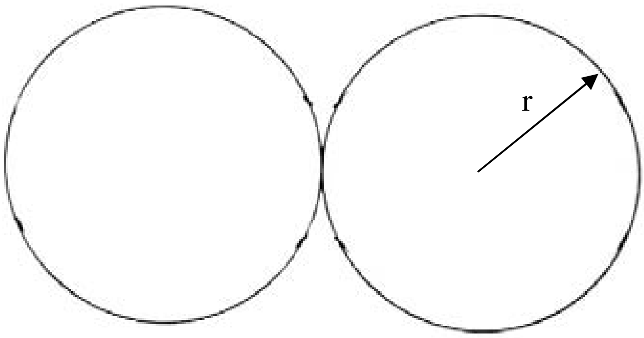

← No Shrinkage →

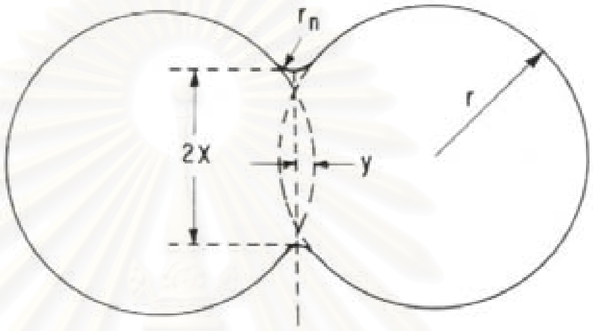

← Shrinkage →

Figure 2.3 Mechanism of sintering; *X* is the internal radius of the neck; *r* is the particle radius.

2.6 Dense perovskite membranes for oxygen separation

One interesting point of perovskite oxides is the presence of oxygen nonstoichiometry by doping process when the B- site ion can take a mixed oxidation state and A-site cation is partially substituted by other metal cations with lower oxidation state. The formation of oxygen nonstoichiometry or oxygen vacancy leads to the modification of the properties, especially the conductivity. Doped perovskite oxides, so called “mixed conductors”, exhibit high ionic conductivity as well as high electrical conductivity (usually 2 orders of magnitude higher than ionic conductivity).

Currently, extensive studies are focused on dense membranes made of this type of materials for oxygen permeation. A schematic description of the dense perovskite type membrane is given in Fig. 2.4

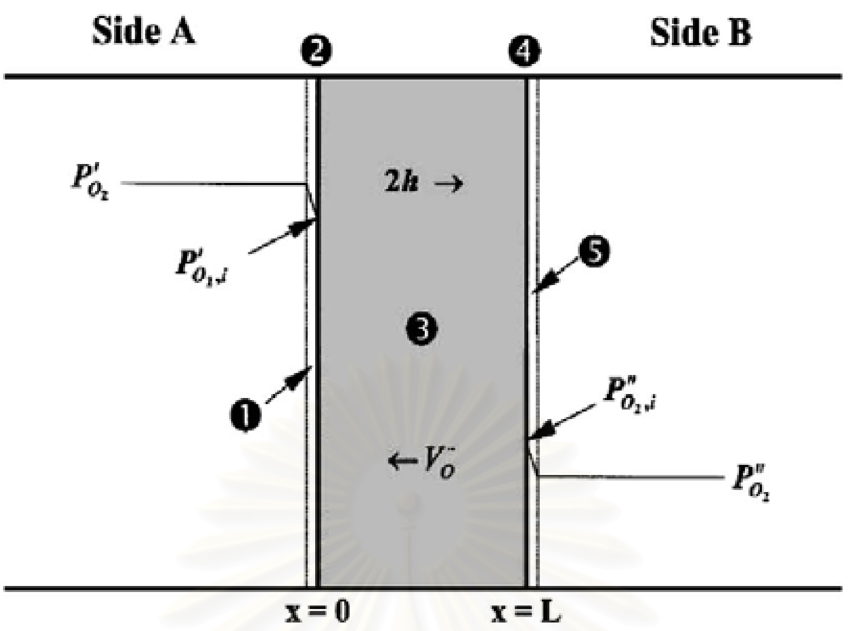

Figure 2.4 Oxygen transport through a perovskite type membrane

In the above diagram, membrane is in the middle, and high and low oxygen pressure zones are, respectively, in the left and right sides of the membrane. The driving force for oxygen transport is the difference of oxygen partial pressures of both sides. High temperature provides the energy for the increasing motion of ions. Following reaction occur at both interfaces of the membrane:

On interface I

$$\frac{1}{2}O_2 + V_O^{\bullet\bullet} \Leftrightarrow O_O^X + 2h^{\bullet} \tag{2.11}$$

The Kröger-Vink notation is used in the above equation, where *V*ö is oxygen vacancy which can be created by doping, $O^x{}_o$ the lattice oxygen, and *h* the electron hole. At high oxygen pressure side, oxygen molecule of gas phase is captured at the interface I and combined with oxygen vacancy, and finally it becomes lattice oxygen. Due to the charge neutrality, electron holes are also produced.

On interface II

$$O_O^X + 2h^{\bullet} \Leftrightarrow \frac{1}{2}O_2 + V_O^{\bullet\bullet} \tag{2.12}$$

The lattice oxygen produced on interface I then transports through the membrane due to its concentration difference. On interface II, lattice oxygen, getting two electron holes, becomes the molecular oxygen by releasing one oxygen vacancy. So, through reaction (1) and (2), oxygen is transport through membrane from the high oxygen pressure zone to the low oxygen pressure zone.

For such mixed-conducting dense membranes, it was well known that the permeation rate of oxygen through mixed conducting film was determined by the magnitude of ionic conduction. Noticeable high ionic conductivity of mixed conductors, such as perovskite-type membranes, prompts the extensive studies on dense ceramic membranes made of these type of materials.

At the steady-state oxygen permeation flux can be readily correlated to P'_{O_2} and P''_{O_2} in an explicit equation [43].

$$J_{O_2} = \frac{D_V k_r (P'^{0.5}_{O_2} - P''^{0.5}_{O_2})}{2Lk_f (P'_{O_2} P''_{O_2})^{0.5} + D_V (P'^{0.5}_{O_2} + P''^{0.5}_{O_2})} \qquad (2.13)$$

Where D_v , k_r and k_f are functions of temperature and the specific properties of the membrane and can be determined by fitting experimental oxygen flux data as a function of temperatures and oxygen partial pressure gradients.

CHAPTER III

EXPERIMENTAL

The apparatus and experimental procedures including processing of perovskite powders synthesis, perovskite membranes preparation and characterization of materials, are described as below:

3.3 Chemicals

The chemicals listed in Table 4.1, were used without further purification.

Table 3.1 Reagents for synthesis of perovskite

Reagents	Formula Weight	Purity%	Company
$La(NO_3)_3{\cdot}6H_2O$	433.02	99.999 99.9 99.9	Aldrich Alfa Sigma
$Ba(NO_3)_2$	261.53	99	Fluka
$Sr(NO_3)_2$	211.63	99.995 99.9965	Aldrich Alfa
$Fe(NO_3)_3{\cdot}9H_2O$	404.00	99.99+ 99.9	Aldrich Sigma
$Co(NO_3)_2{\cdot}6H_2O$	291.03	98	Aldrish
Citric Acid	192.12	99.5+	Aldrich
HNO_3	63.01	70	Lab-Scan
NH_3H_2O	35.05	30	Panreac

3.3 Synthesis of perovskite powder by citrate method

The perovskite oxides, $La_{0.5}Sr_{0.5}Co_{0.6}Fe_{0.4}O_{3-\delta}$ (LSCF5564), $La_{0.6}Sr_{0.4}Co_{0.6}Fe_{0.4}O_{3-\delta}$ (LSCF6464), $La_{0.7}Sr_{0.3}Co_{0.6}Fe_{0.4}O_{3-\delta}$ (LSCF7364), $La_{0.8}Sr_{0.2}Co_{0.6}Fe_{0.4}O_{3-\delta}$ (LSCF8264), $La_{0.8}Sr_{0.2}Co_{0.5}Fe_{0.5}O_{3-\delta}$ (LSCF8255), $La_{0.8}Sr_{0.2}Co_{0.7}Fe_{0.3}O_{3-\delta}$ (LSCF8273), $La_{0.8}Sr_{0.2}Co_{0.8}Fe_{0.2}O_{3-\delta}$ (LSCF8282), $La_{0.8}Sr_{0.2}Co_{0.9}Fe_{0.1}O_{3-\delta}$ (LSCF8291), were synthesized in acidic solution.

Stoichiometric amounts of corresponding high purity metal nitrates (based on 0.02 mole of perovskite powder) were partially dissolved in 10 ml distilled water. Then citric acid with an amount of 1.2 times of the metal solution was added. The mixture solution was stirred at room temperature for 24 hours, and then heated at 96-100°C for 3.5 hours. The solution changed from partially dissolved dark red solution to dark red gel**.**

The combustion of the homogeneous solution was carried out on a hot plate at around 200°C in a three-liter beaker covered with a fine sieve to prevent the loss of fine powders. The water was evaporated until a sticky gel was obtained. Then it became a large swelling viscous mass and finally self ignited by nitrate compound. The combustion lasted for about 10-20 seconds. The solids expanded to occupy almost 1/3 of the beaker volume at the end. The resulting powder was ground by mortar and pestle, and then calcined in the air at 800 ^{o}C for 4 hours with heating rates of 1°C/min to achieve phase purity and eliminate the residual organic compound. The particle was ground completely well by mortar before characterization.

3.3 Synthesis of perovskite powder by modified citrate method

All components, $La_{0.5}Sr_{0.5}Co_{0.6}Fe_{0.4}O_{3-\delta}$ (LSCF5564), $La_{0.6}Sr_{0.4}Co_{0.6}Fe_{0.4}O_{3-\delta}$ (LSCF6464), $Ba_{0.5}Sr_{0.5}Co_{0.6}Fe_{0.4}O_{3-\delta}$ (BSCF5564), $Ba_{0.6}Sr_{0.4}Co_{0.6}Fe_{0.4}O_{3-\delta}$ (BSCF6464), $Ba_{0.7}Sr_{0.3}Co_{0.6}Fe_{0.4}O_{3-\delta}$ (BSCF7364), $Ba_{0.8}Sr_{0.2}Co_{0.6}Fe_{0.4}O_{3-\delta}$ (BSCF8264), $Ba_{0.8}Sr_{0.2}Co_{0.5}Fe_{0.5}O_{3-\delta}$ (BSCF8255), $Ba_{0.8}Sr_{0.2}Co_{0.7}Fe_{0.3}O_{3-\delta}$ (BSCF8273), $Ba_{0.8}Sr_{0.2}Co_{0.8}Fe_{0.2}O_{3-\delta}$ (BSCF8282), $Ba_{0.8}Sr_{0.2}Co_{0.9}Fe_{0.1}O_{3-\delta}$ (BSCF8291), were synthesized in basic solution.

The powder preparation was modified from the citrate pyrolysis method. Stoichiometric amounts of corresponding high purity metal nitrates (based on 0.02 mole of perovskite powder) were partially dissolved in 10 ml ultra pure nitric acid

(70%). Then citric acid with an amount of two times of the total metal ions was added. The mixture solution was then titrated with liq. NH_3 at the controlled rate of 2-3 ml/min. The pH of the solution was adjusted to 8-9. Then the solution changed from partially dissolved brown solution to clear brown solution.

The combustion of the homogeneous solution was carried out on a hot plate at around 200°C in a three-liter beaker covered with a fine sieve to prevent the loss of fine powders. The water was evaporated until a sticky gel was obtained. Then it became a large swelling viscous mass and finally self ignited by NH_4NO_3. The combustion lasted for about 10-20 seconds. The sponge-like solids expanded to occupy almost 2/3 of the beaker volume at the end. The resulting powder was ground by mortar and pestle, and then calcined in the air at 1,000 °C for 5 hours with heating rates of 1°C/min to achieve phase purity and remove the residual carbon. The particle was ground completely well by mortar before characterization.

The equation for the formation of these perovskites assuming complete combustion of the redox mixtures containing citric acid, for example, BSCF, can be written as;

$$(1-x)Ba(NO_3)_3 + xSr(NO_3)_2 + (1-y)Co(NO_3)_3 + yFe(NO_3)_3 + 2HOC(COOH)(CH_2COOH)_2$$

$$\Big\downarrow$$

$$Ba_{1-x}Sr_x Co_{1-y}Fe_yO_{3-\delta}\ (s) + 12CO_2\ (g) + 8H_2O\ (g) + 3N_2\ (g) \tag{3.1}$$

According to Equation (3.1), two moles of citric acid are required to react with 2 moles of all combined metal nitrates. In other words, the total metals will react with citric acid in the approximately equimolar ratio. However, in practice, the excess amount of citric acid was used to assure the complete reaction of all the metal nitrates. Normally, three moles of citric acid was used to react with 2 moles of the total metal nitrates. Therefore, every three molecules of citric acid originally present, one remained uncombined and was removed from the mixture later by either evaporation or decomposition to yield carbon dioxide and water during heating in the vacuum oven. In this research, the citric acid is twice as much as the total metal nitrate, was used in the synthesis of each perovskites.

3.4 Perovskite membrane preparation

A KBr die was used for the shape-forming process, which includes loading, pressing and ejecting. The die cavity was coated by wax then by oil before the perovskite powder was loaded into the cavity but the powders was ground and added with acetone. The die having the perovskite powders inside was knocked against table for 2-3 times to evaporate the air inside the powders. After the die was completely assembled, the plunger was brought to the surface of the powders gently for final leveling and then rotates for smooth surface. About 4-5 tons were then applied on the plunger of the die by the uniaxial pressing machine, which gave pressures about 39,000-56,000 kg/cm^2 on the powders. At the beginning of pressing, the pressure was slowly applied. After 10 minutes, the pressure was released and then the die was removed from the press. All the components were then stripped away except for the die assembly and plunger. Then the assembly was held while the press was slowly pumped until the pellet ejected. The black disc is around 1 mm thick, 13 mm diameter from 350-500 mg of powder, depending on the composition. Then the black discs were generally sintered in air at 1,100-1,300^{o}C for 5 hours with the heating rate 2.0 ^{o}C/min. Finally the sample was cooled to room temperature. Then the black discs change to the dark gray discs.

3.5.1 Calcination and sintering of the perovskite oxides

Calcination and sintering of the perovskite oxides were performed in a Carbolite RHF 1600 muffle furnace in air. The condition used for the calcination and sintering of LSCF and BSCF perovskites were shown in Fig. 3.1 and Fig 3.2, respectively.

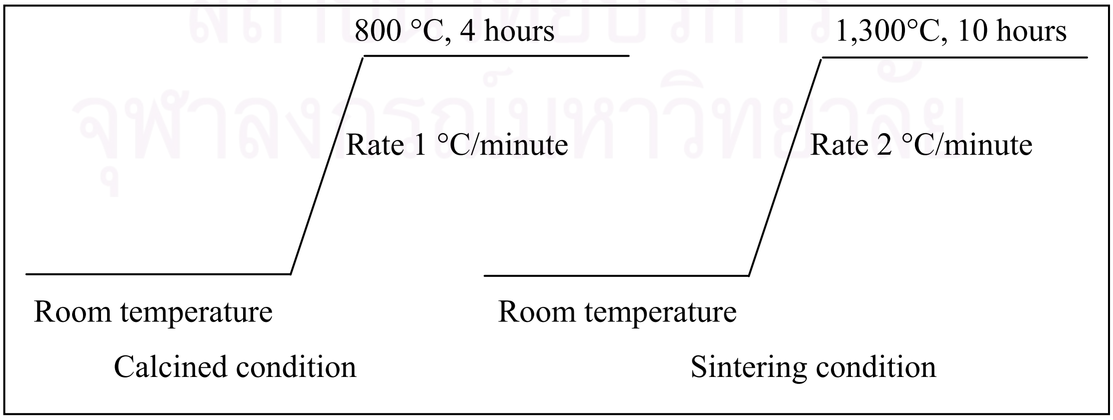

Figure 3.1 The condition used for the calcination and sintering of LSCF.

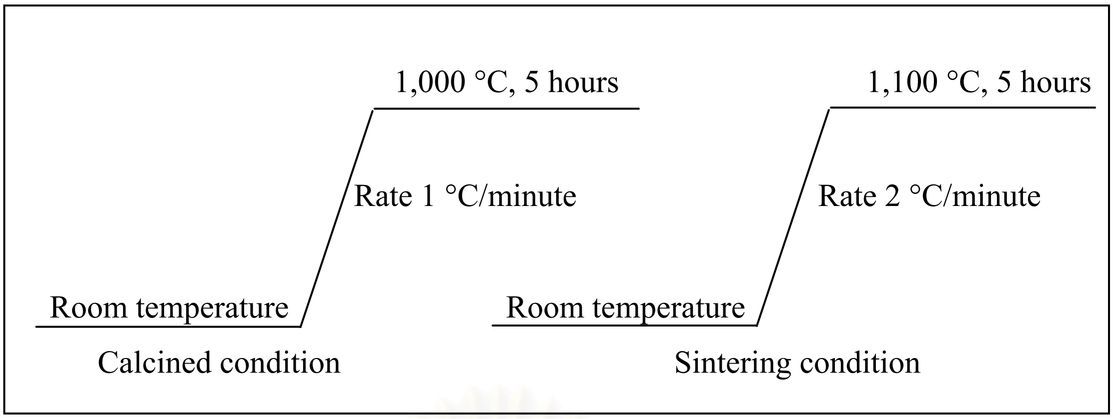
1,000 °C, 5 hours
Rate 1 °C/minute
Room temperature
Calcined condition
1,100 °C, 5 hours
Rate 2 °C/minute
Room temperature
Sintering condition

Figure 3.2 The condition used for the calcination and sintering of BSCF.

3.6 Characterization of the perovskite oxides

3.6.1 X-ray diffractrometry (XRD)

The X-ray patterns, for either powder or membranes, were taken by using Rigaku, DMAX 2002 Ultima Plus X-Ray powder diffractometer eqipped with a monochromator and a Cu-target X-ray tube (40 kV, 30 mA) and angles of 2θ ranged from 20-70 degree at Department of Chemistry, Faculty of Science, Chulalongkorn University.

The phase formations of perovskite powders were characterized after calcination and sintering by XRD.

3.6.2 Scanning electron microscopy (SEM)

The morphology of the membrane discs was carried out using a JEOL JSM-5800LV scanning electron microscopy, Oxford Instrument (Link ISIS series 300) at the Scientific and Technological Research Equipment Center (STREC), Chulalongkorn University. This instrument uses X-rays or electrons scattered back from the surface "illuminated" by a restored electron beam to generate an image with remarkable three-dimensional qualities. Specimens were sputter coated with gold to reduce charge effects.

3.6.3 DENSITY

Density of perovskite membranes was determined by the Archimedes immersion method using water as a medium (model Density Kit), at the Petroleum and Petrochemical College, Chulalongkorn University.

3.6.4 Thermogravimetric analysis (TGA)

Thermogravimetric analysis (TGA, model SDT 2960) was performed on powder specimens from room temperature to 1,000°C using a heating rate of 20 °C/min which was located that Department of Chemistry, Faculty of Science, Mahidol University. The TGA measurements were performed under N_2 atmosphere. In this experiment the perovskite membranes were grounded into fine powder.

3.6.5 Temperature-programmed desorption (TPD)

The perovskite capabilities of adsorbing O_2 were measured using temperature-programmed desorption (TPD, model Thermo Finnigan/TPDRO 1100), at the Petroleum and Petrochemical College, Chulalongkorn University.

The perovskite powder was first pretreated in He atmosphere (30 ml/min) at 500°C for 0.5 hours, then cooled to 100°C, after which adsorption of gas was performed in a flow of O_2 (5.29% balanced by He) for 40 min. The powder was maintained at 100°C in He flow for another 0.5 hours to eliminate physically adsorbed O_2. Thereafter, the TPD was conducted by heating the sample to 800°C at a rate 20°C/min. The desorbed O_2 was analyzed using gas chromatograph with a thermal conductivity detector (TCD).

CHAPTER IV

RESULTS AND DISCUSSIONS

The perovskites-type oxides were prepared by the citrate method or the modified citrate method, each perovskite compound is indicated by the abbreviation using the initial letters of each metal in A and B sites sequentially, followed by the corresponding number which refers to the proportion of each metal in the compound. For examples, $La_{0.8}Sr_{0.2}Co_{0.6}Fe_{0.4}O_{3-\delta}$ and $Ba_{0.8}Sr_{0.2}Co_{0.6}Fe_{0.4}O_{3-\delta}$ are abbreviated as LSCF8264 and BSCF8264, respectively.

4.1 Perovskite powder

4.1.1 Synthesis of LSCF perovskite powder by citrate method

The mixed LSCF systems were prepared via the citrate process. Lanthanum nitrate $La(NO_3)_3.6H_2O$, strontium nitrate, $Sr(NO_3)_2$, cobalt nitrate $Co(NO_3)_2.6H_2O$ and ferrous nitrate $Fe(NO_3)_3.9H_2O$ were dissolved in distilled water, which then react with citric acid to form metal-citrate-nitrate complexes. These metal-citrate complexes can form polymeric precursor when solution is heated at 96-100 ˚C for 3.5 hours. The solution changed from partially dissolved dark red solution to dark red gel**.**

The experimental conditions and data for the synthesis of LSCF (x = 0.2-0.5, y = 0.4) and (x = 0.2, y = 0.1-0.5) perovskite powders were shown in Table 4.1., 4.2, respectively.

Table 4.1 List of the experimental conditions for synthesis of the LSCF ($x = 0.2$-0.5, $y = 0.4$) perovskite compounds

Compounds	Solution color in citric acid	Color and appearance changing during titration	Material feature	Tc (^{o}C)
LSCF 8264	Dark red	Dark red solution to dark red gel	Dark brown powder	800
LSCF 7364	Dark red	Dark red solution to maroon gel	Black powder	800
LSCF 6464	Dark red	Dark red solution to maroon gel	Black powder	800
LSCF 5564	Dark red	Dark red solution to dark red gel	Black gray powder	800

Table 4.2 List of the experimental conditions for synthesis of the LSCF ($x = 0.2$, $y = 0.1$-0.5) perovskite compounds

Compounds	Solution color in citric acid	Color and appearance changed after heated at 96-100 °C for 3.5 hours	Material feature	Tc (^{o}C)
LSCF 8291	Red brown	Red brown solution to dark red brown gel	Dark brown powder	800
LSCF 8282	Dark red	Dark red solution to dark red brown gel	Dark gray powder	800
LSCF 8273	Dark red	Dark red solution to dark red gel	Dark gray powder	800
LSCF 8264	Dark red	Dark red solution to dark red gel	Dark brown powder	800
LSCF 8255	Dark orange	Dark orange solution to dark red gel	Gray brown powder	800

4.1.2 Synthesis of BSCF perovskite powder by modified citrate method

By modified citrate method, the metal nitrates were dissolved in 70% nitric acid, which then reacted with citric acid to form metal-citrate-nitrate complexes. These metal-citrate complexes can under go polymerization when liquid ammonia was added. Meanwhile $NH_3.H_2O$ was added, the white fume of NH_4NO_3 was suddenly observed, which came from the free NO_3^- reacting with $NH_3.H_2O$ and generating the heat. In the case of BSCF, the colour of the mixture had been changed from brown to clear brown at pH≈1 and fume stopped at pH≈1. At this point, the remained citric acid and NH_4NO_3 might dissolve in the solution due to the adding of $NH_3.H_2O$ (10 ml). Then the solution was changed to clear yellow solution (pH≈1.5) and to yellow cloudy solution (pH≈3-6). This solution indicated the metal citrate-nitrate gel resulting from the polymerization of the metal citrate-nitrate complex when $NH_3.H_2O$ was increased. Then the solution was changed form clear yellow brown to clear brown solution (pH≈ 9).

The combustion of the metal citrate-nitrate gel solution was composed of three steps, evaporation, decomposition, and spontaneous combustion. The excess solvent was firstly evaporated until a sticky gel was obtained. During the final stage of evaporation, the mixture began to swell, and became viscous. The generated gases can be observed from the large swelling viscous mass. Finally, at around 200°C the spontaneous combustion was initiated to convert the mixture into the powder [17]. A typical burning of 40 ml of gel solution was completed within 10-20 seconds.

The experimental conditions and data for the synthesis of BSCF perovskite powders with x = 0.2-0.5, y = 0.4 and x = 0.2, y = 0.1-0.5 were shown in Table 4.3. and 4.4, respectively.

Table 4.3 List of the experimental conditions for synthesis of the BSCF (x = 0.2-0.5, y = 0.4) perovskite compounds

Compounds	Solution color		Color and appearance changing during titration	pH	Material feature	Tc (°C)
	Nitric acid	Citric acid				
BSCF 8264	Shocking Pink	Orange Red	Orange red to dark brown	8.70	Dark brown powder	1000
BSCF 7364	Rose color	Orange brown	Orange brown to brilliant red	8.78	Dark brown powder	1000
BSCF 6464	Shocking Pink	Orange brown	Orange brown to dark brown	9.02	Black powder	1000
BSCF 5564	Shocking Pink	Orange brown	Orange brown to dark brown	9.00	Black powder	1000

Table 4.4 List of the experimental conditions for synthesis of the BSCF (x = 0.2, y = 0.1-0.5) perovskite compounds

Compounds	Solution color		Color and appearance changing during titration	pH	Material feature	Tc (^{o}C)
	Nitric acid	Citric acid				
BSCF 8291	Dark red	Orange red	Orange red to dark brown to black	8.85	Black powder	1000
BSCF 8282	Dark red	Orange red	Orange red to dark brown to black	8.94	Dark gray powder	1000
BSCF 8273	Dark red	Orange red	Orange red to dark brown to black	8.83	Black powder	1000
BSCF 8264	Shocking Pink	Orange Red	Orange red to dark brown	8.70	Dark brown powder	1000
BSCF 8255	Shocking Pink	Orange brown	Orange brown to precipitate to dark red to dark brown solution	8.75	Dark brown powder	1000

4.2 Effect of sintering temperature to the formation of LSCF and BSCF

4.2.1 Effect of sintering on the LSCF phase transformation

$La_{1-x}Sr_xCo_{1-y}Fe_yO_{3-\delta}$ perovskite compounds listed Table 4.1 and 4.2 were calcined to eliminate the residue carbon and sintered to obtain the dense membrane. The calcined powder and membranes were characterized by XRD.

Figure 4.1 shows the XRD patterns of LSCF5564 powder after calcined at 800°C for 4 hours and the secondary phase was found. After sintering temperatures at 1,300^{o}C for 10 hours, XRD pattern of membrane shows the single phase. XRD analyses of this powder revealed that the main phase is LSCF, the observed secondary phase formation (marked with▼) could be due to the existence of the oxide compounds such as strontium carbonate ($SrCO_3$) (JCPDS-database:05-0418) [44]. As indicated that the single phase of LSCF5564 perovskite powder was not obtained after calcined at 800°C. The secondary phase disappeared after sintering at 1,300^{o}C. It can be explained that $SrCO_3$ might dissolve into the crystal lattice of LSCF.

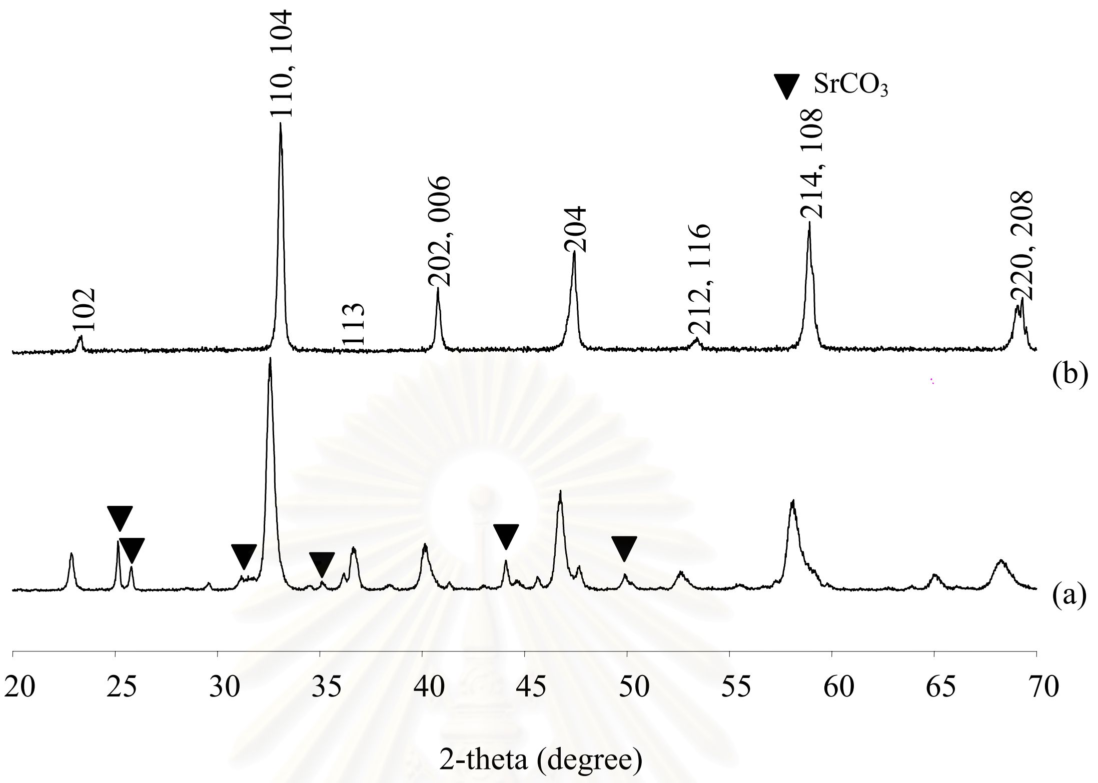

Figure 4.1 XRD patterns of (a) LSCF5564 perovskite powder after calcined at 800°C for 4 hours and (b) LSCF5564 membrane after sintered at 1,300°C for 10 hours.

The all LSCF compositions prepared for this study are listed in Table 4.5. including XRD results from both as-calcined powders and sintered membranes. Sintered membranes were single phase, although the secondary phase as $SrCO_3$ were detected in the calcined powders with $x \geq 0.3$.

Table 4.5 XRD analyses of calcined powder and the sintered membranes of LSCF (at 25°C)

Samples	Calcined temperature (°C)	Phase of the calcined powders	Sintering temperature (°C)	Phase symmetry of sintered perovskite structure
LSCF5564	800	Perovskite + $SrCO_3$	1,300	Orthorhombic
LSCF6464	800	Perovskite + $SrCO_3$	1,300	Orthorhombic
LSCF7364	800	Perovskite + $SrCO_3$	1,300	Rhombohedral
LSCF8255	800	Perovskite	1,300	Rhombohedral
LSCF8264	800	Perovskite	1,300	Rhombohedral
LSCF8273	800	Perovskite	1,300	Rhombohedral
LSCF8282	800	Perovskite	1,300	Rhombohedral
LSCF8291	800	Perovskite	1,300	Rhombohedral

4.2.2 Effect of sintering on the BSCF phase transformation

The X-ray diffraction patterns of as-calcined powder and sintered membrane BSCF7364 at room temperature is shown in Figure 4.2. There are some peaks at 2θ of about 31° in calcined powder. Based on a search of the database and literature, the peak from secondary phase can not be assigned to any known compounds. However, The trace of secondary phase was eliminated after sintering at 1,100^{o}C. All peaks can be given a Miller index of a cubic structure, showing that the main peaks at 2θ of about 22, 32, 38, 46, 52, 57, 66 and 70°. This was due to the cubic perovskite having the diffraction lines 100, 110, 111, 200, 210, 211, 220 and 221.

Table 4.6 lists all $Ba_{1-x}Sr_xCo_{1-y}Fe_yO_{3-\delta}$ compositions that were prepared including XRD results from calcined powders and sintered membrane. All of the sintered membranes were exhibited to be single phase except BSCF8282 and BSCF8291. They have $BaFeO_{2.9}$ (JCPDS-database:23-1024) [45] as the secondary phase. $BaFeO_{2.9}$ is stable at high temperature. Therefore, $BaFeO_{2.9}$ still appeared withBSCF8291 and BSCF8282 after sintering.

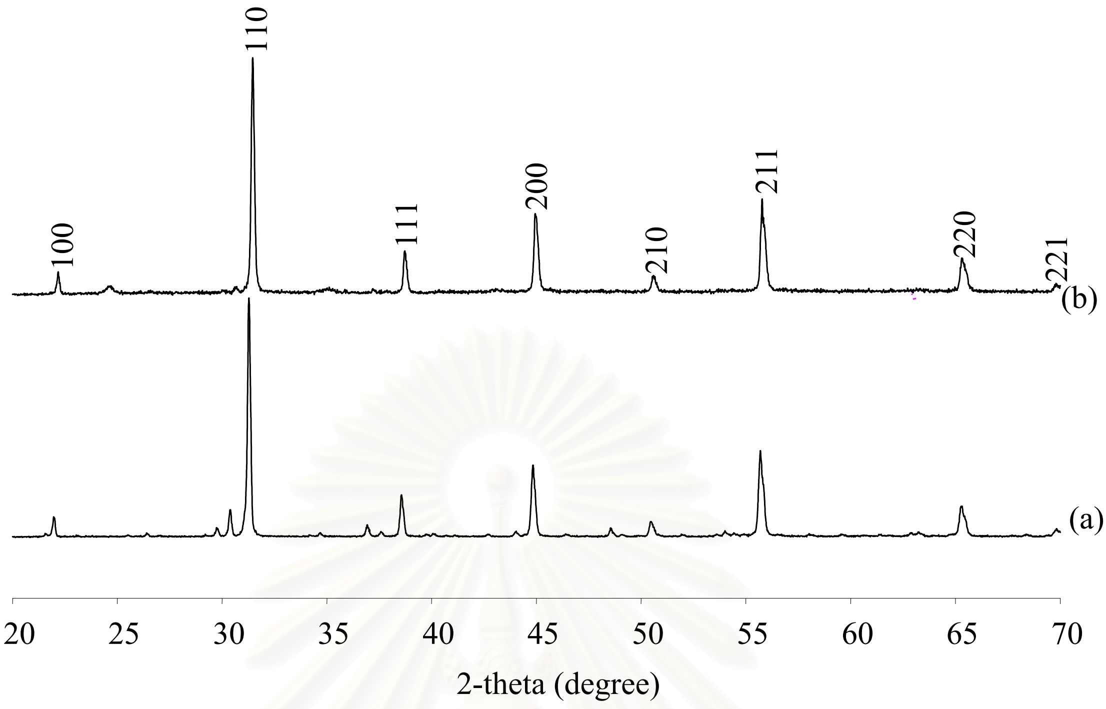

Figure 4.2 XRD patterns of (a) BSCF7364 perovskite powder after calcined at 1,000^{o}C for 5 hours and (b) BSCF7364 membrane after sintered at 1,100^{o}C for 5 hours.

Table 4.6 XRD analyses of calcined powders and the sintered membranes of BSCF (at 25°C)

Samples	Calcined temperature (°C)	Phase of the calcined powders	Sintering temperature (°C)	Phase symmetry of sintered perovskite structure
BSCF5564	1,000	Perovskite	1,100	Cubic
BSCF6464	1,000	Perovskite	1,100	Cubic
BSCF7364	1,000	Perovskite + 2nd phase	1,100	Cubic
BSCF8255	1,000	Perovskite	1,100	Cubic
BSCF8264	1,000	Perovskite	1,100	Cubic
BSCF8273	1,000	Perovskite	1,100	Cubic
BSCF8282	1,000	Perovskite + $BaFeO_{2.9}$	1,100	Cubic + $BaFeO_{2.9}$
BSCF8291	1,000	Perovskite + $BaFeO_{2.9}$	1,100	Cubic + $BaFeO_{2.9}$

4.3 The influence of A-site and B-site cations on the formation of perovskite oxides

4.3.1 Effect of composition on the formation of LSCF-based perovskite

In this section, Two series of LSCF perovskites, $La_{0.8}Sr_{0.2}Co_{1-y}Fe_yO_{3-\delta}$ (y = 0.1, 0.2, 0.3, 0.4, 0.5) and $La_{1-x}Sr_xCo_{0.6}Fe_{0.4}O_{3-\delta}$ (x = 0.2, 0.3, 0.4, 0.5), were investigated by XRD technique.

4.3.1.1 The variation of Sr contents in $La_{1-x}Sr_xCo_{0.6}Fe_{0.4}O_{3-\delta}$ (x = 0.2, 0.3, 0.4, 0.5)

The XRD patterns of samples after calcination were recorded at room temperature. Basically, the XRD pattern of the single-phase perovskite with a rhombohedral structure will exhibit the diffraction lines at the reflective planes 012, 110, 104, 113, 202, 006, 024, 122, 116, 300, 214, 108, 220 and 208. For a $La_{1-x}Sr_xCo_{0.6}Fe_{0.4}O_{3-\delta}$, these reflective lines appear as the peak at 2θ = 23, 32.5, 33, 39, 40.5, 41, 47, 53, 53.5, 58.5, 58.7, 59, 68.5, 69.5 degree.

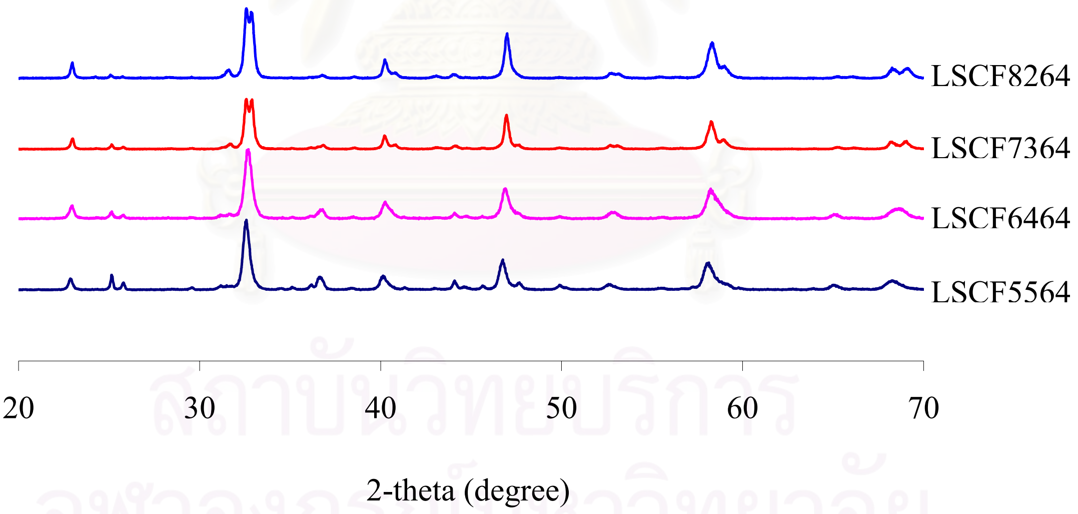

Figure 4.3 XRD patterns of LSCF5564, LSCF6464, LSCF7364 and LSCF8264 perovskite powders after calcined at 800 ^{o}C for 4 hours.

In addition, the XRD patterns of LSCF perovskite powder when y = 0.4 and various Sr contents showed other small peaks appeared at 2θ = 25, 31, 36.5, 43, 44, 65, 66 degree, indicating the secondary phase ($SrCO_3$) in the structure. The amount of the secondary phase was slightly increased with increasing of Sr contents. However, the impurities disappeared when LSCF membranes were sintered at 1,300°C, as illustrated in Figure 4.4.

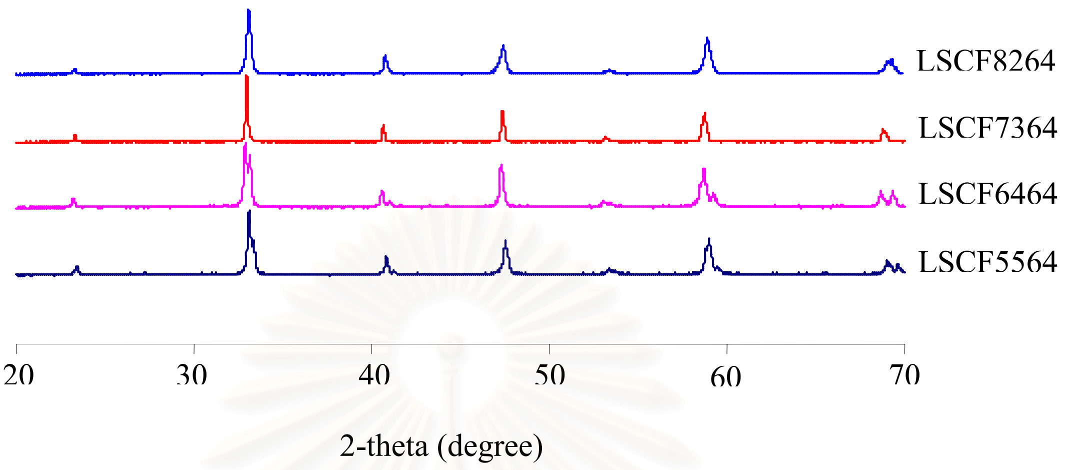

Figure 4.4 XRD patterns of LSCF5564, LSCF6464, LSCF7364 and LSCF8264 perovskite membrane after sintering at 1,300 °C for 10 hours.

For compositions with Sr ≥ 0.4 the orthorhombic phase was stable at room temperature, while Sr ≤ 0.3 the rhombohedral phase was identified by XRD. The partial XRD patterns of LSCF with various Sr contents showed that LSCF crystal structures changed from rhombohadral to orthorhombic structure with increasing amount of Sr contents, as illustrated in Figure 4.5.

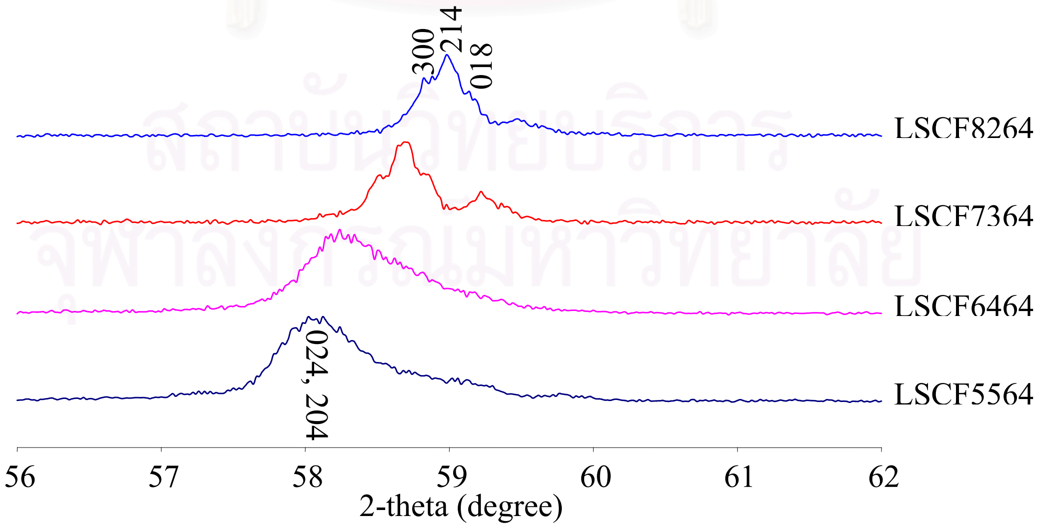

Figure 4.5 Partial XRD patterns of LSCF membranes with various Sr contents.

From Table 4.7, the unit cell volumes were calculated from the lattice parameters. From the same structure, LSCF7364 has more the unit cell volume than LSCF8264. In addition, LSCF5564 has higher unit cell volume than LSCF6464. As a result, the dimensions of ABO_3 unit cell increase with increasing amount of Sr contents. Because the substitution of La^{3+} (r = 1.36 Å) by Sr^{2+} (r = 1.44 Å) in $La_{1-x}Sr_xCo_{0.6}Fe_{0.4}O_{3-\delta}$ induced the average radius of A ions to increase.

Table 4.7 Crystallographic data for LSCF perovskite various Sr contents

Sample	Crystal system	a/ Å	b/ Å	c/ Å	Cell Volume/ Å ^{3}
LSCF5564	Orthorhombic	3.8839	3.8879	3.9121	59.0736
LSCF6464	Orthorhombic	3.8682	3.8720	3.8967	58.3635
LSCF7364	Rhombohedral	5.4594	5.4594	13.0813	337.6536
LSCF8264	Rhombohedral	5.4037	4.4037	13.0637	330.3538

4.3.1.2 The variation of Fe contents in $La_{0.8}Sr_{0.2}Co_{1-y}Fe_yO_{3-\delta}$ (y = 0.1, 0.2, 0.3, 0.4, 0.5)

$La_{0.8}Sr_{0.2}Co_{1-y}Fe_yO_{3-\delta}$ (y = 0.1, 0.2, 0.3, 0.4, 0.5) were characterized by XRD (Figure 4.7). For $La_{0.8}Sr_{0.2}Co_{1-y}Fe_yO_{3-\delta}$ series, it was found that $La_{0.8}Sr_{0.2}Co_{1-y}Fe_yO_{3-\delta}$ series are rhombohedral structure for $0.1 \leq y \leq 0.5$ at room temperature.

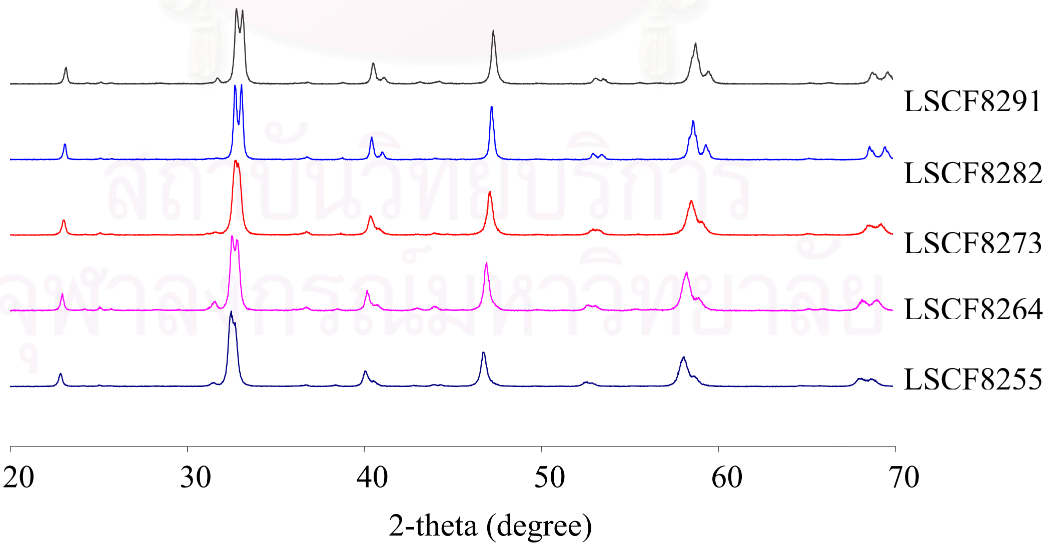

Figure 4.6 XRD patterns of LSCF8291, LSCF8282, LSCF8273, LSCF8264 and LSCF8255 perovskite powders after calcined at 800 °C for 4 hours.

From the XRD patterns in Figure 4.7, it is demonstrated that at room temperature the perovskite phase of $La_{0.8}Sr_{0.2}Co_{1-y}Fe_yO_{3-\delta}$ has a rhombohedral symmetry for $0.1 \leq y \leq 0.5$. It appears that the substitution of Co^{2+}(r = 0.65 °A) by Fe^{3+}(r = 0.55 °A) diminished the average radius of B ions. In agreement with Roth [45], who suggested that perovskite-type ABO_3, structures with smaller B ions are more stable in the rhombohedral symmetry than in the orthorhombic structure. The unit cell parameters and volumes are exhibited in Table 4.8. It can be concluded that the unit cell volumes of LSCF decreased with increasing Fe contents with $0.1 \leq y \leq 0.4$.

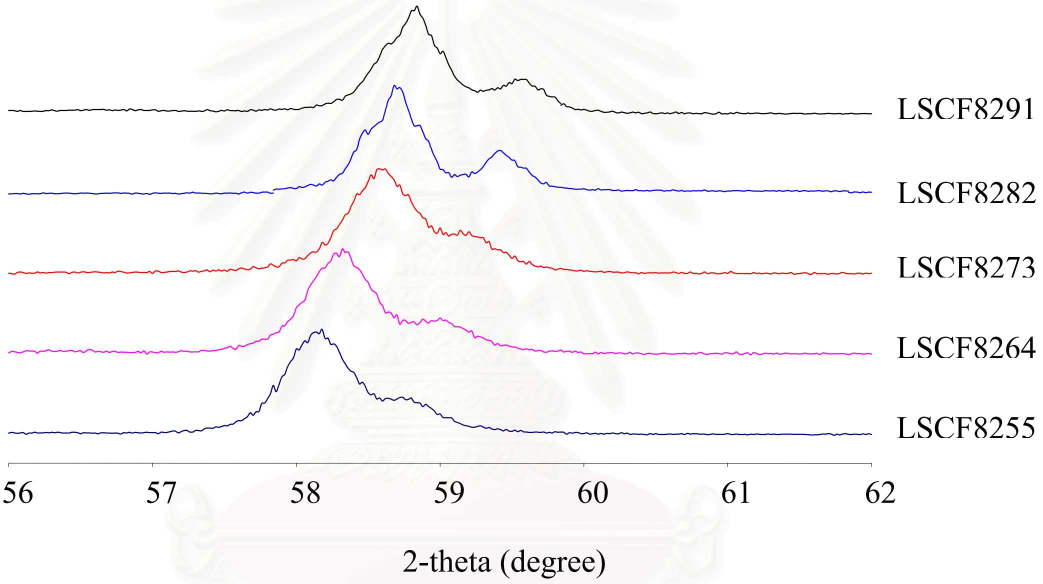

Figure 4.7 Partial XRD patterns of LSCF membranes with various Fe contents.

Table 4.8 Crystallographic data for LSCF perovskite various Fe contents

Sample	Crystal system	a/ Å	b/ Å	c/ Å	Cell Volume/ $Å^3$
LSCF8291	Rhombohedral	5.4521	5.4521	13.1503	338.5275
LSCF8282	Rhombohadral	5.4354	5.4354	13.1156	335.5690
LSCF8273	Rhombohedral	5.4157	5.4157	13.0746	332.0995
LSCF8264	Rhombohedral	5.4037	5.4037	13.0637	330.3538
LSCF8255	Rhombohedral	5.4463	5.4463	13.1390	337.5173

4.3.2 Effect of composition on the formation of BSCF-based perovskite

The variation of Sr and Fe contents on the BSCF perovskite formation was characterized by XRD patterns. Two series of BSCF perovskites, $Ba_{0.8}Sr_{0.2}Co_{1-y}Fe_yO_{3-\delta}$ (y = 0.1, 0.2, 0.3, 0.4, 0.5) and $Ba_{1-x}Sr_xCo_{0.6}Fe_{0.4}O_{3-\delta}$ (x = 0.2, 0.3, 0.4, 0.5), were studied in this section.

4.3.2.1 The variation of Sr contents in $Ba_{1-x}Sr_xCo_{0.6}Fe_{0.4}O_{3-\delta}$ (x = 0.2, 0.3, 0.4, 0.5)

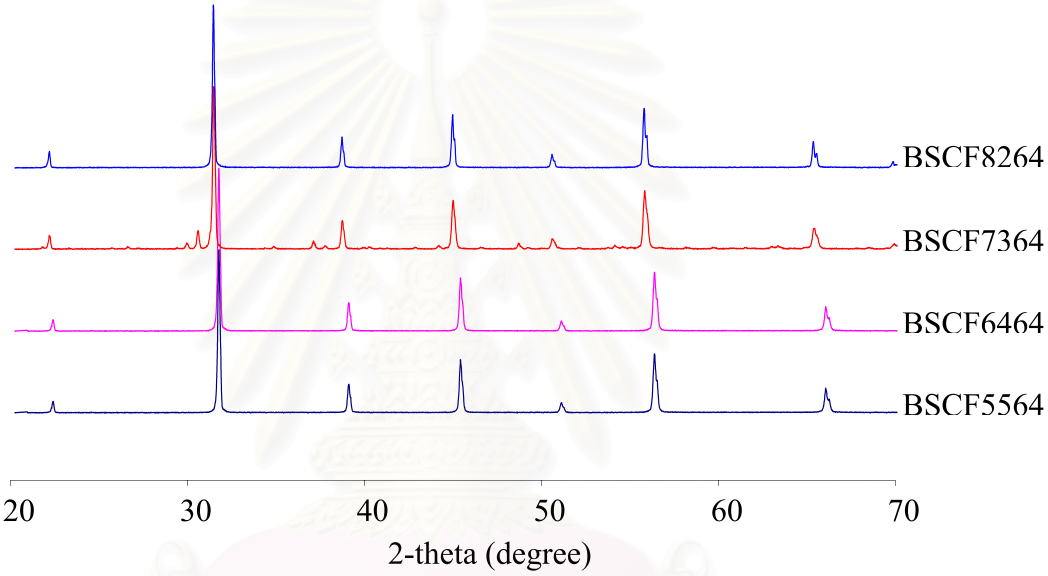

Figure 4.8 XRD patterns of BSCF5564, BSCF6464, BSCF7364 and BSCF8264 perovskite powders after calcined at 1,000 °C for 5 hours.

The XRD patterns of BSCF 8264, BSCF6464 and BSCF5564 exhibited the single phase of perovskite. As shown in Figure 4.8, the trace of secondary phase was observed in BSCF7364. It has some trivial unidentified peaks at 2θ of about 31°. The unidentified compound in BSCF7364 was eliminated after the membrane was sintered. The XRD patterns of the single-phase BSCF membranes with cubic structure exhibit the diffraction lines at the reflective planes 100, 110, 111, 200, 210 and 211. For a $Ba_{1-x}Sr_xCo_{0.6}Fe_{0.4}O_{3-\delta}$, these reflective lines appear as peaks at 2θ = 22, 31, 38.5, 39, 45, 50 degree. Therefore, all XRD patterns in Figure 4.9 clearly indicate that all synthesized BSCF membranes with various Sr have the cubic structure.

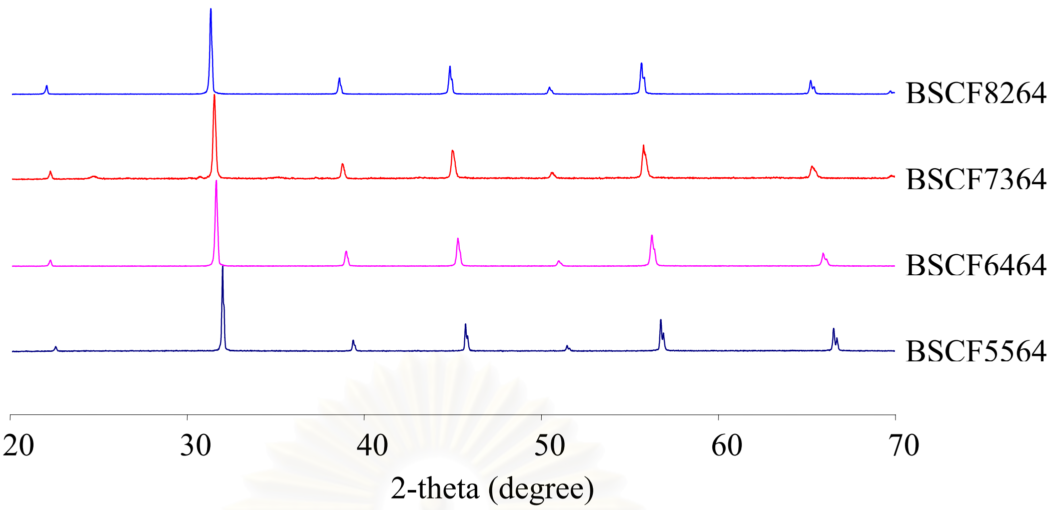

Figure 4.9 XRD patterns of BSCF5564, BSCF6464, BSCF7364 and BSCF8264 perovskite membranes after sintering at 1,100 ^{o}C for 5 hours.

The lattice parameter (a) has been calculated for each X values, in $Ba_{1-x}Sr_xCo_{0.6}Fe_{0.4}O_{3-\delta}$ system, from the six most intensive diffraction peaks of the cubic structure shown in Table 4.9. The substitution of Ba^{2+} (ionic radius = 1.61 Å) by Sr^{2+} (ionic radius = 1.44 Å) in $Ba_{1-x}Sr_xCo_{0.6}Fe_{0.4}O_{3-\delta}$ diminished the averaged radius of A ions in the perovskite structure. Therefore, the unit cell volumes decreased with increasing amount of Sr^{2+} in BSCF.

Table 4.9 Crystallographic data for BSCF perovskite with various Sr contents

Sample	Crystal system	a/ Å	b/ Å	c/ Å	Cell Volume/ A^{o3}
BSCF5564	Cubic	3.9635	3.9635	3.9635	62.2639
BSCF6464	Cubic	4.0033	4.0033	4.0033	64.1585
BSCF7364	Cubic	4.0335	4.0335	4.0335	65.6215
BSCF8264	Cubic	4.0415	4.0415	4.0415	66.0127

4.3.2.2 The variation of Fe contents in $Ba_{0.8}Sr_{0.2}Co_{1-y}Fe_yO_{3-\delta}$ (y = 0.1, 0.2, 0.3, 0.4, 0.5)

Figure 4.10 shows the XRD patterns of the BSCF series of y = 0.1-0.5. Based on the calculation on the torelance factor for the perovskite structure, the result showed that it was difficult to prepare BSCF materials with pure perovskite phase due to the concentration of $Fe \leq 0.2$ mol ratio. The secondary phase corresponding to the peaks at 2θ of about 28 and 43 degree is identified as $BaFeO_{2.9}$. However BSCF8255, BSCF8264 and BSCF8273 with almost pure perovskite structure were successfully synthesized. They have cubic perovskite structure.

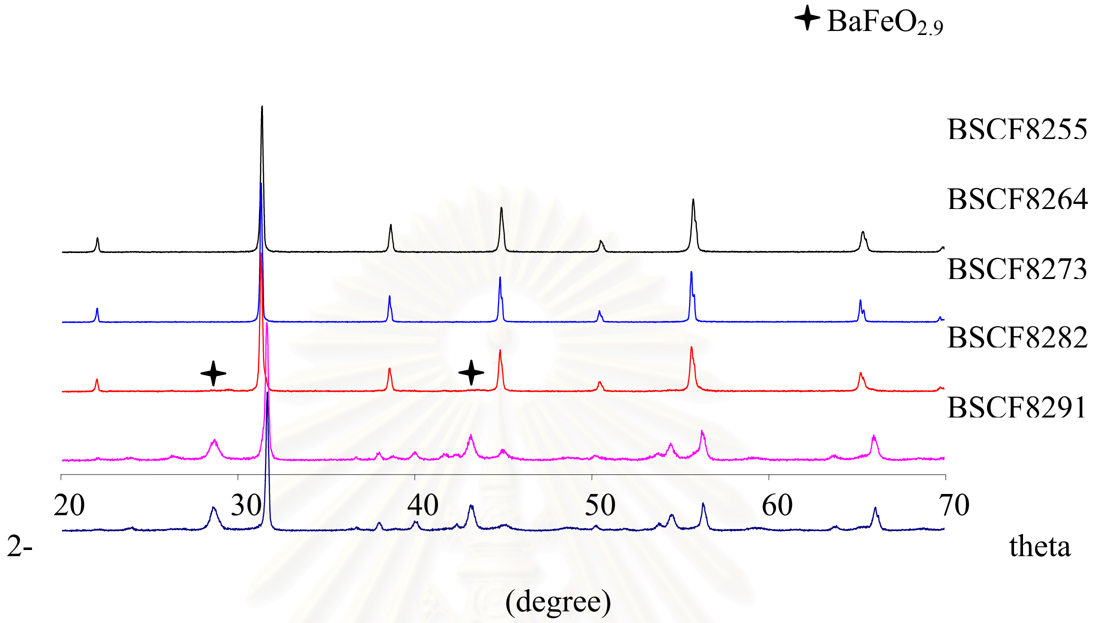

Figure 4.10 XRD patterns of BSCF8255, BSCF8264, BSCF8273, BSCF8282 and BSCF8291 perovskite powders after calcined at 1,000 °C for 5 hours.

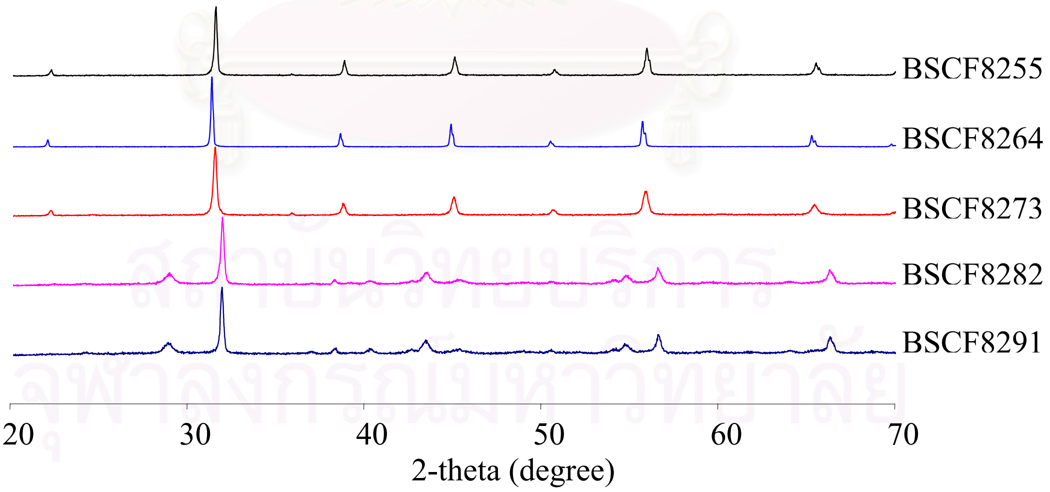

Figure 4.11 XRD patterns of BSCF8255, BSCF8264, BSCF8273, BSCF8282 and BSCF8291 perovskite membrane after sintering at 1,100 °C for 5 hours.

The XRD patterns of BSCF membranes with various Fe contents were shown in Fig 4.11. The crystal structures of $Ba_{0.8}Sr_{0.2}Co_{1-y}Fe_yO_{3-\delta}$ did not change after sintered. For BSCF8282 and BSCF 8291, the intensity of $BaFeO_{2.9}$ peak decreased when the temperature increased to 1,100°C. This may be due to the partial dissolution of $BaFeO_{2.9}$ into BSCF structure at high temperature.

The crystal structure data of BSCF8273, BSCF8264 and BSCF8255 were shown in Table 4.10. The effect of Fe contents on the cell volume of BSCF series can not be deduced from this data.

Table 4.10 Crystallographic data for BSCF perovskite various Fe contents

Sample	Crystal system	a/ Å	b/ Å	c/ Å	Cell Volume/ $Å^3$
BSCF8291	Cubic + $BaFeO_{2.91}$	-	-	-	-
BSCF8282	Cubic + $BaFeO_{2.91}$	-	-	-	-
BSCF8273	Cubic	4.0245	4.0245	4.0245	65.1832
BSCF8264	Cubic	4.0415	4.0415	4.0415	66.0127
BSCF8255	Cubic	4.0185	4.0185	4.0185	64.8921

4.4 Effect of composition on the morphology of perovskite membrane

In this section, the morphologies of perovskite membranes at different compositions of Sr and Fe in LSCF and BSCF were studied by SEM technique.

4.4.1 Effect of Sr-contents on the morphologies of LSCF perovskite membranes

The cross section of $La_{1-x}Sr_xCo_{0.6}Fe_{0.4}O_{3-\delta}$ ($x = 0.2$-0.5) membranes were investigated by SEM technique. The morphologies of LSCF8264, LSCF7364, LSCF6464 and LSCF5564 membranes after sintering at 1,300 °C for 10 hours are presented in Figure 4.12.

SEM micrographs of cross section membranes clearly showed that the average grain size increased from 4, 5, 7 and 9 μm with increasing of Sr content in $La_{1-x}Sr_xCo_{0.6}Fe_{0.4}O_{3-\delta}$ system where $x = 0.2$, 0.3, 0.4 and 0.5, respectively. Therefore, at the same sintering temperature, the grain size of LSCF increases with increasing Sr compositions.

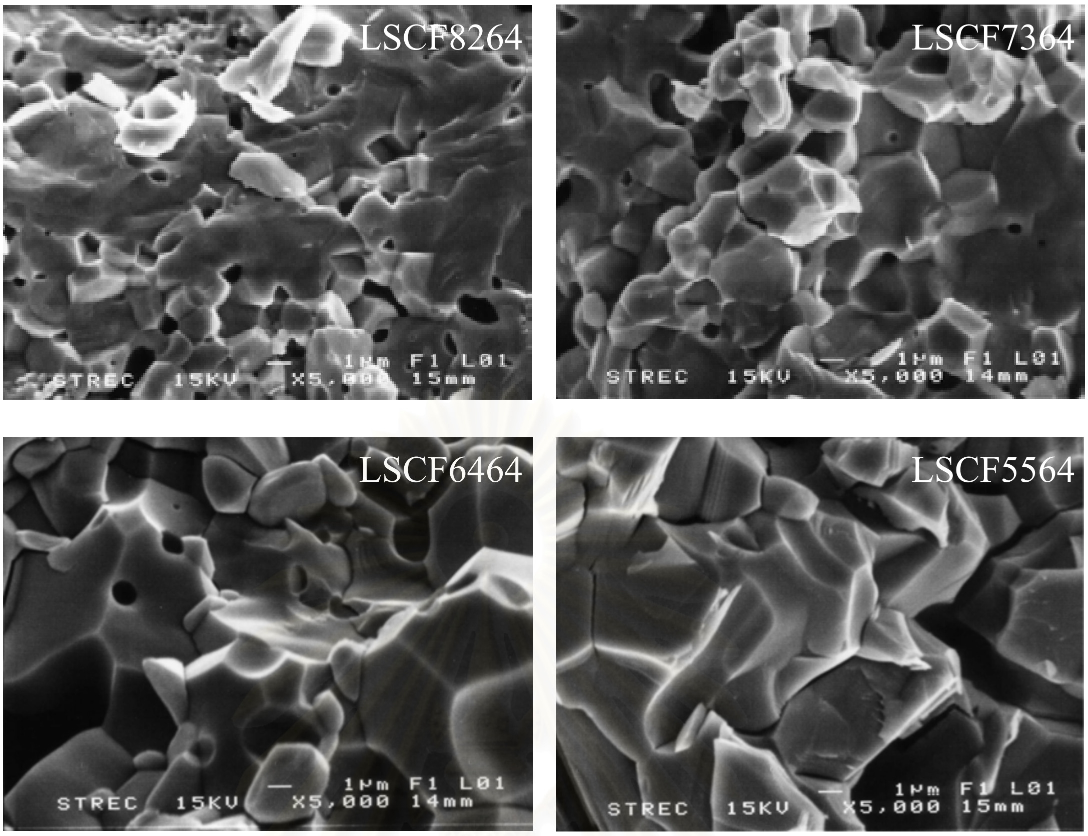
LSCF8264
1µm F1 L01
STREC 15KV X5,000 15mm
LSCF7364
1µm F1 L01
STREC 15KV X5,000 14mm
LSCF6464
1µm F1 L01
STREC 15KV X5,000 14mm
LSCF5564
1µm F1 L01
STREC 15KV X5,000 15mm

Figure 4.12 SEM pictures of cross section of LSCF5564, LSCF6464, LSCF7364 and LSCF8264 samples sintered at 1,300°C for 10 hours.

Density of samples determined by the Archimedes immersion method using water as a medium, were listed in Table 4.11. The grain growth phenomenon was supported by the density result. It is implied that the density of LSCF membrane increased with an increasing amounts of Sr and LSCF5564 has the highest density.

Table 4.11 Density of $La_{1-x}Sr_xCo_{0.6}Fe_{0.4}O_{3-\delta}$ membranes when x = 0.2, 0.3, 0.4 and 0.5

LSCF membrane	Density/g.cm^3
LSCF8264	5.2595
LSCF7364	5.2676
LSCF6464	5.8234
LSCF5564	5.9103

4.4.2 Effect of Fe-contents on the morphologies of LSCF perovskite membranes

The cross section of $La_{0.8}Sr_{0.2}Co_{1-y}Fe_yO_{3-\delta}$ membranes were investigated by SEM technique shown in Figure 4.13. The morphologies of membranes were considered when varied Fe-contents, LSCF8291, LSCF8282, LSCF8273, LSCF8264 and LSCF8255 membranes after sintering at 1,300°C for 10 hours.

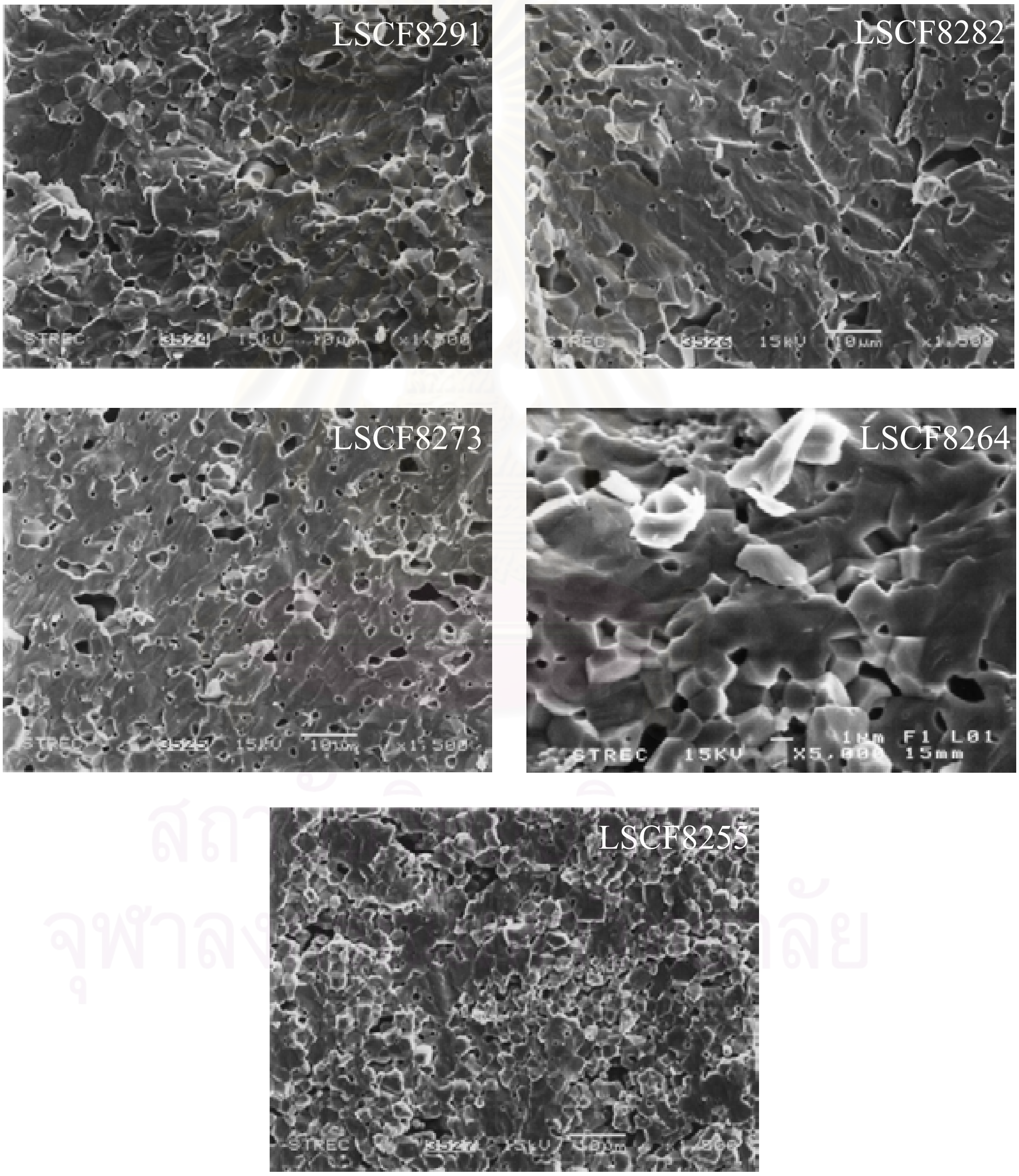
LSCF8291
STREC 15kV 10µm x1,500
LSCF8282
STREC 15kV 10µm x1,500
LSCF8273
STREC 15kV 10µm x1,500
LSCF8264
1µm F1 L01
STREC 15kV X5,000 15mm
LSCF8255
STREC 15kV 10µm

Figure 4.13 SEM pictures of cross section of LSCF8291, LSCF8282, LSCF8273, LSCF8264 and LSCF8255 samples sintered at 1,300°C for 10 hours.

Figure 4.13 shows that the average grain size of $La_{0.8}Sr_{0.2}Co_{1-y}Fe_yO_{3-\delta}$ membranes where y = 0.1, 0.2, 0.3, 0.4 and 0.5 were 6, 8, 9, 4 and 5 μm, respectively. Therefore the Fe contents in LSCF system did not affect on the grain size of membrane after sintering.

Density of samples calculated by the Archimedes immersion method, were listed in Table 4.12. In this section, LSCF8282 has highest density.

Table 4.12 Density of $La_{0.8}Sr_{0.2}Co_{1-y}Fe_yO_{3-\delta}$ membranes when y = 0.1, 0.2, 0.3, 0.4 and 0.5

Sample	Density/ $g.cm^3$
LSCF8291	5.3626
LSCF8282	6.0016
LSCF8273	5.8516
LSCF8264	5.2595
LSCF8255	5.2009

4.4.3 Effect of Sr-contents on the morphologies of BSCF perovskite membranes

The morphology of single-phase membranes of $Ba_{1-x}Sr_xCo_{0.6}Fe_{0.4}O_{3-\delta}$ system type BSCF5564, BSCF6464, BSCF7364 and BSCF8264 was also examined in this section. It can be seen from Figure 4.14 that BSCF membranes show a fusion state in their cross-section. The average grain size of their membranes was around 10 μm.The results clearly demonstrated that Sr contents affect the grain size, when decreasing Sr concentration in BSCF many large closed pores were still observed. In addition, the closed pores caused the decrease of the membrane density. Therefore, the density of BSCF gradually decreased with Sr contents.

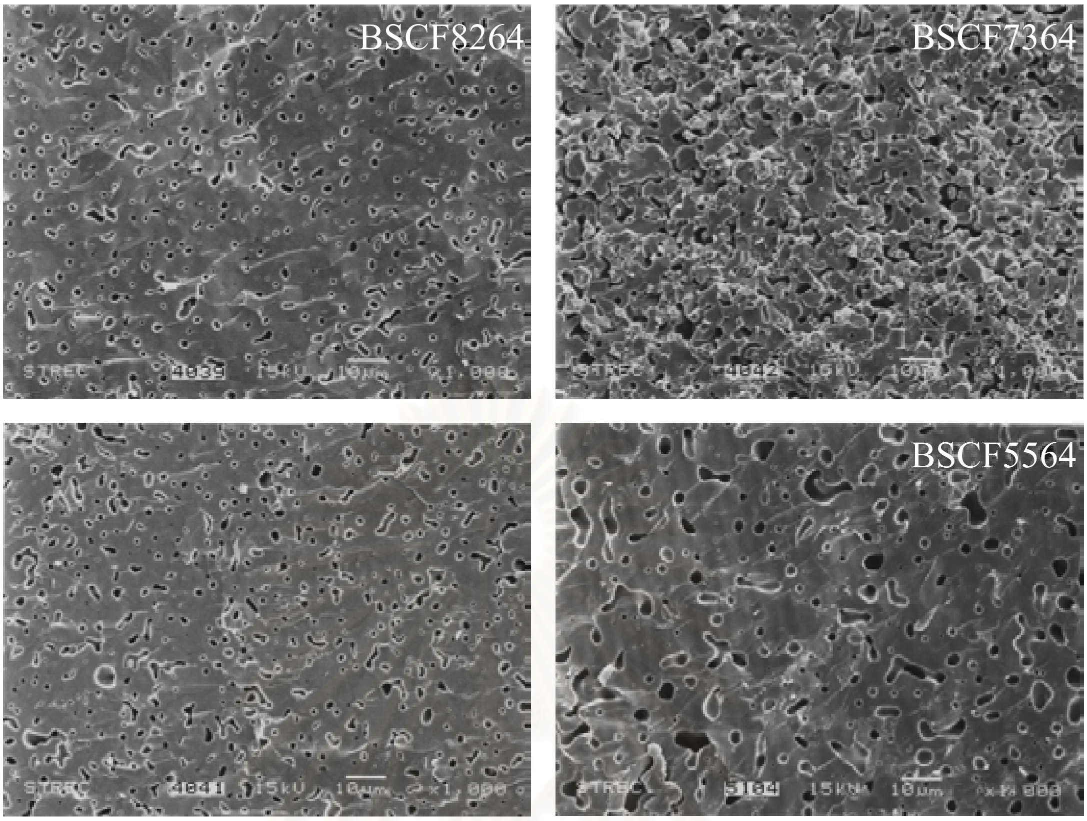

Figure 4.14 SEM pictures of cross section of BSCF8264, BSCF7364, BSCF6464 and BSCF5564 membranes sintered at 1,100°C for 10 hours.

The densities of BSCF with various amount of Sr were listed in Table 4.13. BSCF6464 has highest density.

Table 4.13 Density of $Ba_{1-x}Sr_xCo_{0.6}Fe_{0.4}O_{3-\delta}$ membranes when x = 0.2, 0.3, 0.4 and 0.5

BSCF membrane	Density/g.cm^3
BSCF8264	4.3492
BSCF7364	4.0844
BSCF6464	4.6455
BSCF5564	4.6251

4.4.4 Effect of Fe-contents on the morphologies of BSCF perovskite membranes

The morphologies of $Ba_{0.8}Sr_{0.2}Co_{1-y}Fe_yO_{3-\delta}$ membranes type BSCF8291, BSCF8282, BSCF8273, BSCF8264 and BSCF8255 were also considered in this section. It can be seen from Figure 4.15 that BSCF membranes show a fusion state in their cross-section. The average grain size of their membranes was around 10 µm. BSCF8255 has larger closed pores more than the others. And BSCF8282 has the smallest closed pores. It can be confirmed that BSCF8282 has a highest density, listed in Table 4.14.

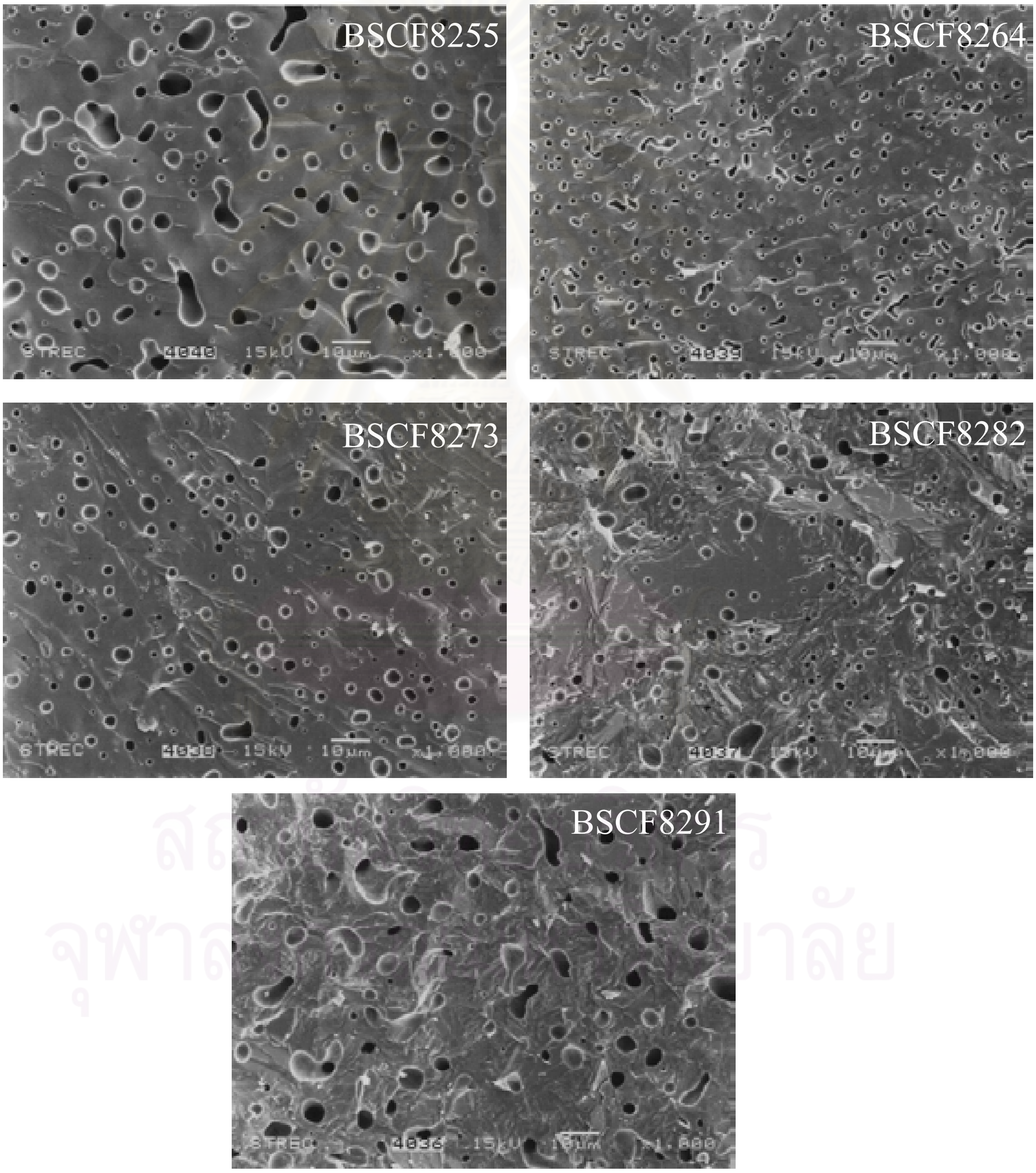
BSCF8255
STREC 4040 15kU 10µm x1,000
BSCF8264
STREC 4039 15kU 10µm x1,000
BSCF8273
STREC 4038 15kU 10µm x1,000
BSCF8282
STREC 4037 15kU 10µm x1,000
BSCF8291
STREC 4036 15kU 10µm x1,000

Figure 4.15 SEM pictures of cross section of BSCF8255, BSCF8264, BSCF8273 BSCF8282 and BSCF8291 membranes sintered at 1,100°C for 5 hours.

Density of $Ba_{0.8}Sr_{0.2}Co_{1-y}Fe_yO_{3-\delta}$ determined by the Archimedes method were listed in Table 4.14, It can be suggested that Fe contents in BSCF did not effect the density of BSCF.

Table 4.14 Density of $Ba_{0.8}Sr_{0.2}Co_{1-y}Fe_yO_{3-\delta}$ membranes when y = 0.1, 0.2, 0.3, 0.4 and 0.5

Sample	Density/ $g.cm^3$
BSCF8291	5.3626
BSCF8282	5.4573
BSCF8273	4.4569
BSCF8264	4.3492
BSCF8255	4.6411

4.5 Thermal Analysis

Thermogravimetric analyses of LSCF and BSCF compositions, with Sr = 0.2-0.5 and Fe = 0.1-0.5 mole ratio, were performed under nitrogen gas (N_2). TG runs were performed at a constant heat rate 10°C/min.

4.5.1 $La_{1-x}Sr_xCo_{0.6}Fe_{0.4}O_{3-\delta}$ compositions with x = 0.2-0.5

Thermogravimetric analyses of LSCF compositions with Sr = 0.2-0.5 were performed under N_2. The weight loss observed upon heating under N_2 are shown in Figure 4.16. The weights of LSCF changed rapidly at 700°C for x = 0.2-0.4 and 300°C for x = 0.5. The weight loss is the result of the lattice oxygen loss in LSCF perovskite. It can be seen that, LSCF8264, LSCF7364 and LSCF6464 are more stable than LSCF5564 since their oxygen deficiency are lower than those of LSCF5564. Therefore, the extent of oxygen loss increases with increasing Sr content in LSCF. It appears that the A-site acceptor dopant plays a substantial role in determining the thermal stability of the lattice oxygen. This observation is consistent with the findings reported by Tai et al. [46, 47] on oxygen adsorption/desorption and catalytic properties of some other compositions in LSCF. They concluded that total amount of oxygen desorbed from LSCF increased with Sr content.

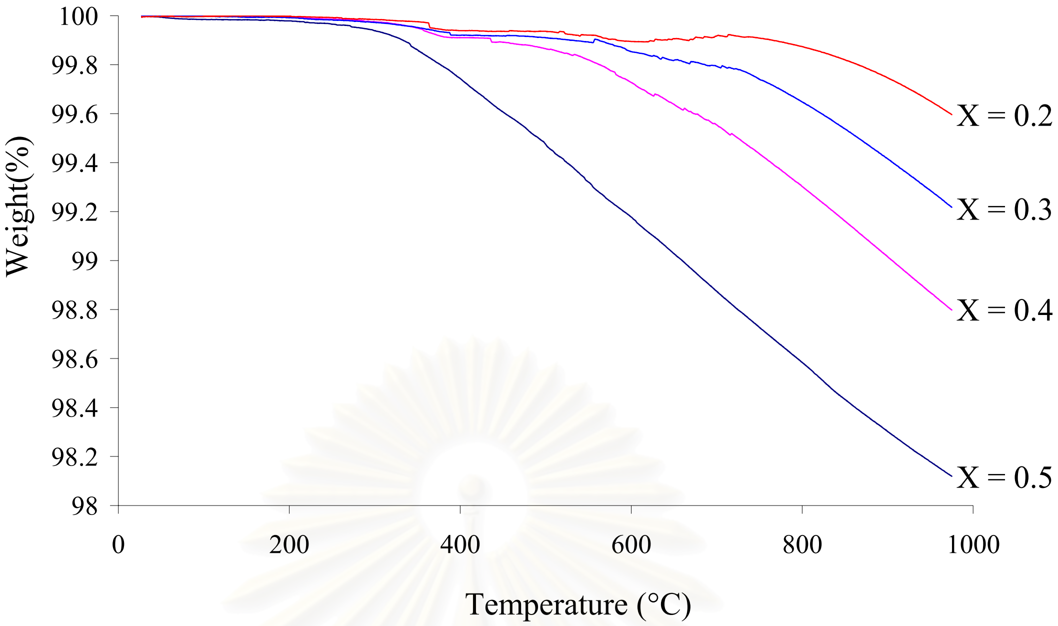

Figure 4.16 Relative weight loss of $La_{1-x}Sr_xCo_{0.6}Fe_{0.4}O_{3-\delta}$ as function of temperatures and Sr content under N_2.

By considering the room temperature oxygen contents and the TG weight loss data. The oxygen content for each composition can be calculated at high temperature under N_2. The oxygen deficiency increased with increasing Sr content and temperature. Table 4.15 lists oxygen contents for compositions with Sr = 0.2-0.5 at 900°C. It can be inferred the oxygen non-stoichiometry of LSCF perovskite compounds in creased with increasing the amount of Sr contents.

Table 4.15 Oxygen non-stoichiometry (δ) in $La_{1-x}Sr_xCo_{0.6}Fe_{0.4}O_{3-\delta}$ for x = 0.2-0.5 at room temperature and 900°C under N_2

X (mol)	Oxygen non-stoichiometry at room temperature (δ)	Oxygen non-stoichiometry at 900°C (δ′)	Δδ
0.2	0.400	0.4064	0.0064
0.3	0.4500	0.4648	0.0148
0.4	0.5000	0.5246	0.0246
0.5	0.5500	0.5916	0.0416

4.5.2 $La_{0.8}Sr_{0.2}Co_{1-y}Fe_yO_{3-\delta}$ compositions with y = 0.1-0.5

The weight changes for LSCF powder samples with various Fe contents were almost completely heating under N_2 atmosphere. It is suggested that the observed weight change results from the loss of lattice oxygen on heating. TG weight losses for LSCF compositions with Fe = 0.1-0.5 upon heating under N_2 are plotted versus temperature in Figure 4.17.

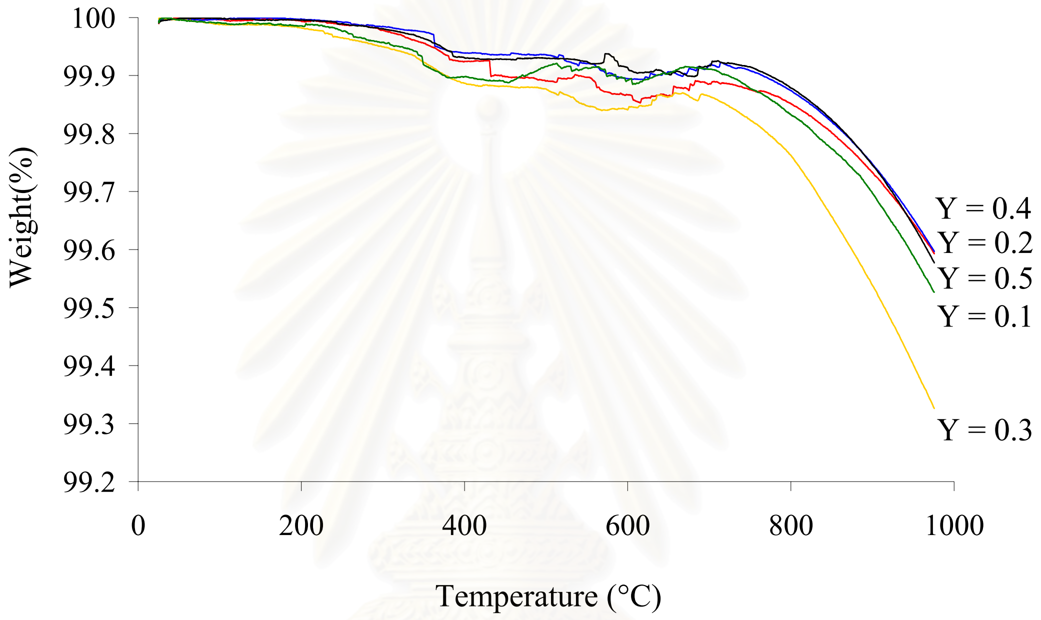

Figure 4.17 Relative weight loss of $La_{0.8}Sr_{0.2}Co_{1-y}Fe_yO_{3-\delta}$ as function of temperatures and Fe contents under N_2.

From Figure 4.17, The samples have abnormal weight change in the range of 300-700°C and lost the weight rapidly at 700-1,000°C. As the temperature increases, LSCF perovskite lose oxygen from the lattice by the so-called desorption of β-oxygen. Most of the TGA curves show dramatic decreases starting around 700°C suggesting that both desorption of β-oxygen and the reduction of the Fe and Co ions from higher to lower valences may occur.

By combining the room temperature oxygen contents and the TG weight loss data. The oxygen content for each composition can be calculated at high temperature under N_2. The oxygen deficiency increased with increasing the Fe content and temperature. Table 4.16 lists oxygen contents for compositions with Fe = 0.1-0.5 at

900°C. The Δδ value of LSCF8273 perovskite compound was higher than those of the others. It can be implied that LSCF8273 showed the highest oxygen permeability.

Table 4.16 Oxygen non-stoichiometry (δ) in $La_{0.8}Sr_{0.2}Co_{1-y}Fe_yO_{3-\delta}$ for y = 0.1-0.5 at room temperature and 900°C under N_2

Y (mol)	Oxygen non-stoichiometry at room temperature (δ)	Oxygen non-stoichiometry at 900°C (δ')	Δδ
0.1	0.5500	0.5572	0.0072
0.2	0.5000	0.5063	0.0063
0.3	0.4500	0.4617	0.0117
0.4	0.4000	0.4064	0.0064
0.5	0.3500	0.3568	0.0068

4.5.1 $Ba_{1-x}Sr_xCo_{0.6}Fe_{0.4}O_{3-\delta}$ compositions with x = 0.2-0.5

Thermogravimetric analyses on BSCF compositions with Sr = 0.2-0.5 were performed under N_2 atmosphere. The weight losses observed upon heating in N_2 are shown in Figure 4.18.

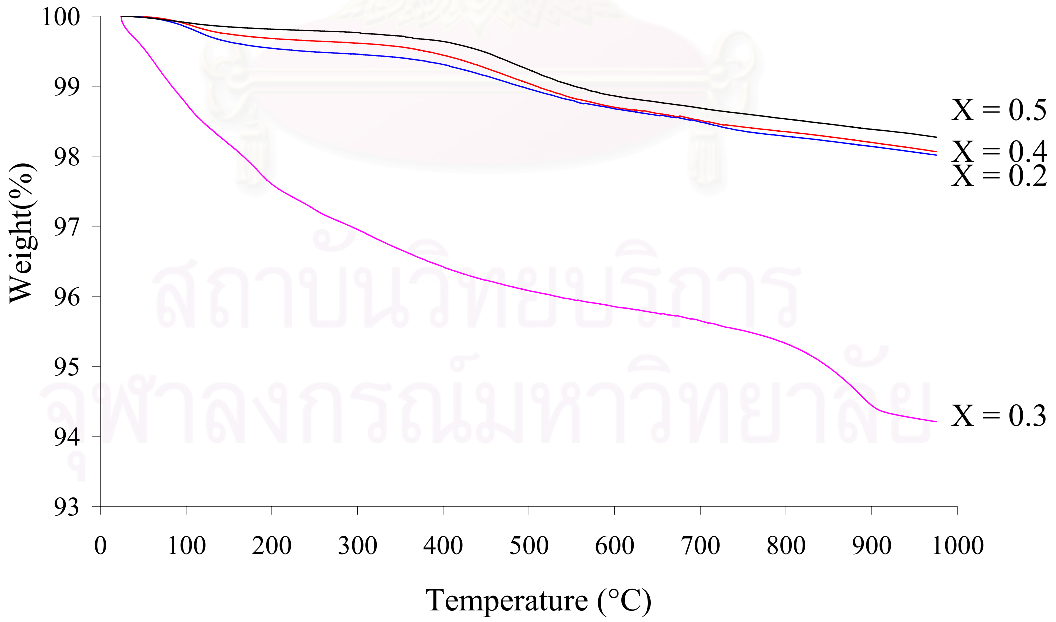

Figure 4.18 Relative weight loss of $Ba_{1-x}Sr_xCo_{0.6}Fe_{0.4}O_{3-\delta}$ as function of temperatures and Sr contents under N_2.

From TGA curves, it can be seen that BSCF7364 has dramatically weight loss starting at room temperature. On the contrary, BSCF8264, BSCF6464 and BSCF5564 have the same weight loss starting around 350°C. The effect of the substitution of Sr contents on the loss of oxygen lattice in BSCF system can not be concluded.

The oxygen contents for BSCF compositions with Sr = 0.2-0.5 at 900°C are listed Table 4.17. Surprisingly, BSCF7364 appeared to lose a lot of oxygen lattice as compared to the others. It can be suggested that BSCF7364 had excellent great oxygen permeability.

Table 4.17 Oxygen non-stoichiometry in $Ba_{1-x}Sr_xCo_{0.6}Fe_{0.4}O_{3-\delta}$ for x = 0.2-0.5 at room temperature and 900°C under N_2

X (mol)	Oxygen non-stoichiometry at room temperature (δ)	Oxygen non-stoichiometry at 900°C (δ')	Δδ
0.2	0.80	0.8410	0.0410
0.3	0.80	0.9223	0.1223
0.4	0.80	0.8396	0.0396
0.5	0.80	0.8356	0.0356

4.5.4 $Ba_{0.8}Sr_{0.2}Co_{1-y}Fe_yO_{3-\delta}$ compositions with y = 0.1-0.5

Figure 4.19 shows the relatively weight loss and the temperature under N_2 atmosphere for BSCF8291, BSCF8282, BSCF8273, BSCF8264 and BSCF8255. The relative weight loss of BSCF8291 and BSCF8282 are different from the others. They have $BaFeO_{2.9}$ as the secondary phase, so their TGA curves may include BSCF and $BaFeO_{2.9}$. However, the weight loss of BSCF8273, BSCF8264 and BSCF8255 have two steps starting at 100°C and 350°C. From BSCF8273, BSCF8264 and BSCF8255 TGA data, it can be suggested that the oxygen deficiency increases with increasing temperature and Fe contents in BSCF.

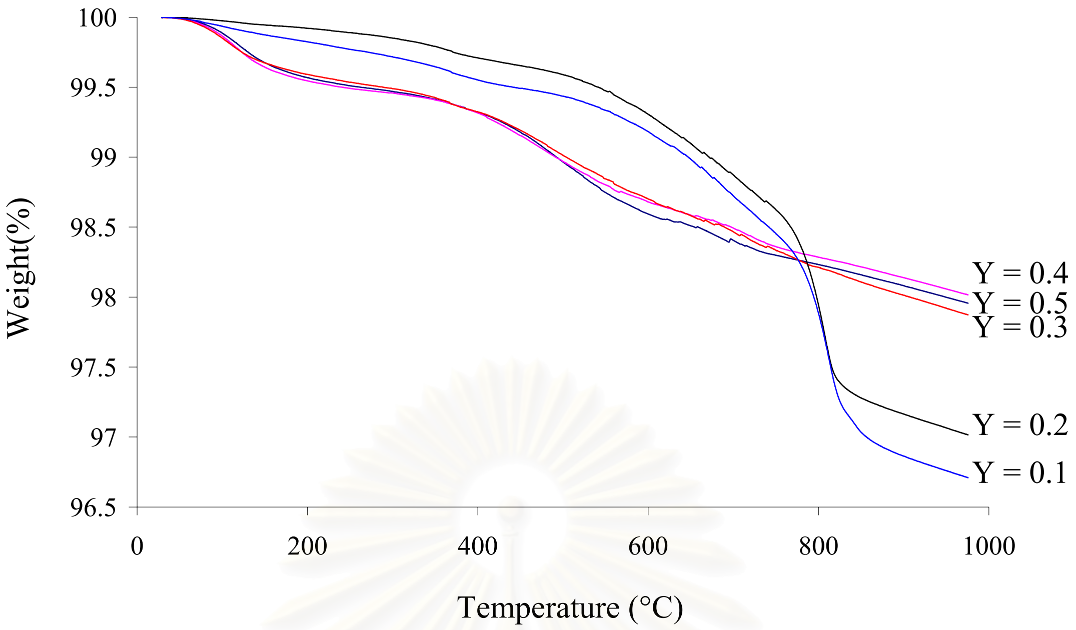

Figure 4.19 Relative weight loss of $Ba_{1-x}Sr_xCo_{0.6}Fe_{0.4}O_{3-\delta}$ as function of temperatures and Fe contents under N_2.

By combining the room temperature oxygen contents and the TG weight loss data. The oxygen deficiency increased with increase of Fe contents and temperature. Table 4.18 lists oxygen contents for compositions with Fe = 0.1-0.5 at 900°C.

Table 4.18 Oxygen non-stoichiometry (δ) in $Ba_{0.8}Sr_{0.2}Co_{1-y}Fe_yO_{3-\delta}$ for y = 0.1-0.5 at room temperature and 900°C under N_2

Y (mol)	Oxygen non-stoichiometry at room temperature (δ)	Oxygen non-stoichiometry at 900°C (δ')	$\Delta\delta$
0.1	0.9500	1.0143	0.0643
0.2	0.9000	0.9595	0.0595
0.3	0.8500	0.8927	0.0427
0.4	0.8000	0.8409	0.0409
0.5	0.7500	0.7931	0.0431

It is interesting to infer that the oxygen vacancy can be calculated from the TGA plots recorded under N_2. As the temperature increases, the perovskite phase loses oxygen from the lattice, and the δ value increases. The oxygen permeability tends to increase with increasing the δ value [5]. Therefore, the oxygen vacancy is useful to predict the oxygen permeability of perovskite. BSCF8291 has highest oxygen vacancy even though it has secondary phase.

4.6 Oxygen temperature-programmed desorption (TPD)

The adsorption/desorption property of the perovskite catalyst plays an important role in the partial oxidation of methane (POM) reaction and TPD is usually an effective method to obtain such information. The O_2-TPD profiles for LSCF8264 and BSCF8264 were shown in Fig. 4.21. It is noted that there are two kinds of oxygen, the so-called α and β-oxygen. The α-oxygen are the oxygen in atmosphere, their desorption occurred below 600°C. In addition, the β-oxygen are the oxygen lattice in perovskite structure, they are desorbed around 600-1000°C. In order to compare the oxygen permeability of La-based and Ba-based perovskite systems, LSCF8264 and BSCF8264 have been selected to investigated their property.

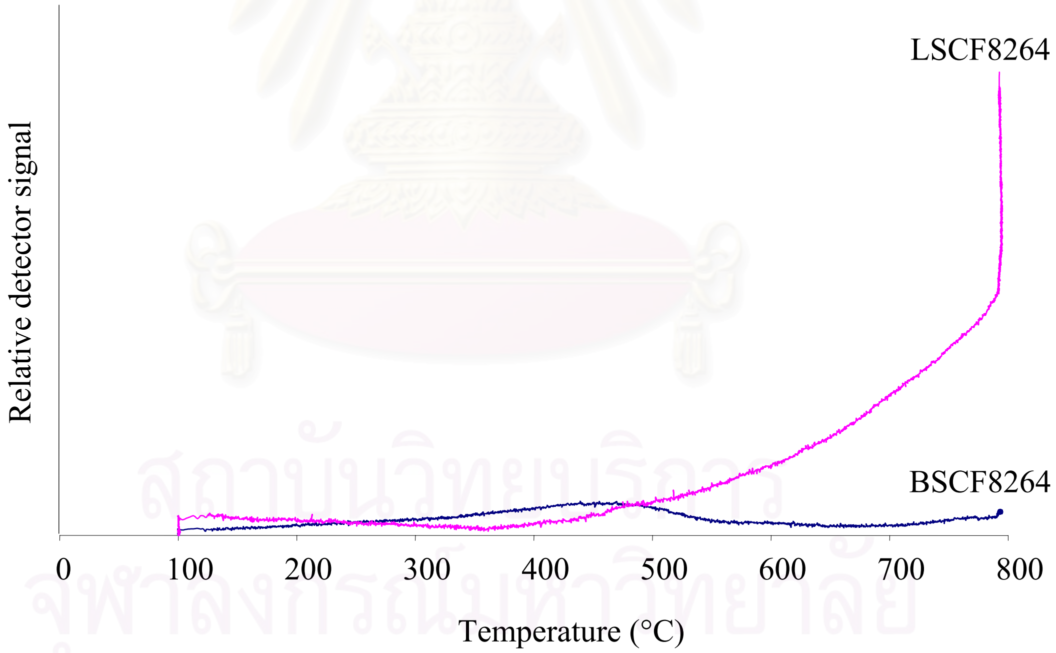

Figure 4.20 O_2-TPD patterns of LSCF8264 and BSCF8264.

From Figure 4.20, the desorption peaks α-oxygen of both occur at low temperature range from 100-350 and 100-550°C for LSCF8264 and BSCF8264, respectively. The amount of β-oxygen was desorbed only in LSCF8264 compound. It is suggested that LSCF8264 has better O_2 adsorption/desorption property more than that of BSCF8264.

CHAPTER V

CONCLUSIONS

The perovskite-type oxides in the system $La_{1-x}Sr_xCo_{1-y}Fe_yO_{3-\delta}$ and $Ba_{1-x}Sr_xCo_{1-y}Fe_yO_{3-\delta}$ were investigated with various compositions of low Sr and Fe contents. The trace amount of impurity phase was presented in Lanthanum-based perovskite with calcination at 800°C. The single phase powder was obtained from Barium-based perovskite calcinined at 1,000°C. The lattice parameter estimated from the XRD analysis was calculated to investigate the influence of A and B-site cation on the lattice parameter as shown in Table 4.7-4.10. The lattice parameter was varied, according to the size of ionic cation.

Fine particle strontium and iron substituted lanthanum cobaltates $La_{1-x}Sr_xCo_{1-y}Fe_yO_{3-\delta}$, where Sr = 0.2-0.5 and Fe = 0.4, Sr = 0.2 and Fe = 0.1-0.5 had been synthesized by a citrate method. In addition, $Ba_{1-x}Sr_xCo_{1-y}Fe_yO_{3-\delta}$ systems were synthesized by a modified citrate process with the same of strontium and iron contents.

Form the XRD patterns of perovskite powders, it was found that LSCF8255, LSCF8264, LSCF8273, LSCF8282 and LSCF8291 were the single phase and the secondary phase observed in LSCF5564, LSCF6464 and LSCF7364. It indicated that the secondary phase occured when the amount of Sr ≥ 0.3 in LSCF. For compositions with Sr ≥ 0.4 the orthorhombic phase was stable at room temperature, while Sr ≤ 0.3 the rhombohedral phase was identified by XRD. It can be concluded that LSCF crystal structures changed from rhombohadral to orthorhombic structure with increasing amount of Sr content.

For $Ba_{1-x}Sr_xCo_{1-y}Fe_yO_{3-\delta}$ powder, the XRD analysis shows that BSCF5564, BSCF6464, BSCF7364, BSCF8255, BSCF8264 and BSCF8273 were the single cubic phase, BSCF8282 and BSCF8291 were observed with $BaFeO_{2.9}$ as the secondary phase. This means that the secondary phase increased when decreasing the amount of Fe contents in BSCF.

The lattice parameters of LSCF and BSCF were calculated from the XRD data show that the unit cell volumes enlarge with increasing amount of Sr contents in

LSCF series. On the other hand, the unit cell volumes decreased with increasing amount of Sr^{2+} in BSCF systems. In addition, the unit cell volumes of $La_{0.8}Sr_{0.2}Co_{1-y}Fe_yO_{3-\delta}$ ($0.1 \leq y \leq 0.4$) decreased with increasing Fe contents. But the effect of Fe contents on the cell volume of BSCF series can not be deduced from this data.

The membranes were prepared by pressing the perovskite powders using a uniaxial pressing machine to form a disc and sintering at 1,100-1,300°C for 10 hours. The membranes characterized by SEM to obtain the microstructure and densification and microstructure. The structure of all perovskite membranes did not changed the structure after sintering. The density of perovskite membrane after sintering was determined by the Archimedes immersion method. It can be concluded that the density of membrane increased with increasing amount of Sr and Co.

The highest dense single-phase perovskite membranes in each composition were concluded in Table 5.1.

Table 5.1 The highest dense perovskite membranes in each composition

Composition	Sintering temperature (^oC)	Density (g/cm^3)	Single-phase
LSCF5564	1,300	5.9103	Yes
LSCF8282	1,300	6.0016	Yes
BSCF6464	1,100	4.6455	Yes
BSCF8282	1,100	5.4573	No

From thermogravimetric analyses of LSCF and BSCF compositions, it can be calculated the oxygen non-stoichiometry for each composition at high temperature under N_2. The oxygen deficiencies for the family of $La_{1-x}Sr_xCo_{0.6}Fe_{0.4}O_{3-\delta}$ perovskite membranes were in the order LSCF5564 > LSCF6464 > LSCF7364 > LSCF8264. For $La_{0.8}Sr_{0.2}Co_{1-y}Fe_yO_{3-\delta}$ system, the oxygen vacancies were in the sequence LSCF7364 >> LSCF8291 > LSCF8255 > LSCF8264 ≈ LSCF8282. It can be inferred that LSCF system, the oxygen deficiencies increased with increasing Sr content but Fe contents did not affect the oxygen vacancies. In addition, $Ba_{1-x}Sr_xCo_{0.6}Fe_{0.4}O_{3-\delta}$ series, the oxygen non-stoichiometry values were in the order BSCF7364 > BSCF8264 > BSCF6464 > BSCF5564. For $Ba_{0.8}Sr_{0.2}Co_{1-y}Fe_yO_{3-\delta}$ family, the oxygen vacancies were in the order of BSCF8291 > BSCF8282 > BSCF8273 > BSCF8264. It can be concluded that the substitution of Sr in BSCF systems did not cause the oxygen deficiencies but the oxygen vacancies increased with decreasing the Fe contents.

Experimental results of O_2-TPD reveal that the amount of O_2 desorbed from LSCF8264 is far larger than BSCF8264 in the range of 500-800°C.

REFERENCES

1. Teraoka, Y.; Nobunaga, T.; Okamoto, K.; Miura, N.; Yamazoe, N. “Influence of Constituent Metal Cations in Substituted $LaCoO_3$ on Mixed Conductivity and Oxygen Permeability”, *Solid State Ionics*, **1991**, *48*, 207-212.
2. van Doorn, R. H. E.; Bouwmeester, H. J. M.; Burggraaf, A. J. “Kinetic Decomposition of $La_{0.3}Sr_{0.7}CoO_{3-\delta}$ Perovskite Membranes During Oxygen Permeation”, *Solid State Ionics*, **1998**, *111*, 263-272.
3. Petric, A.; Huang P.; Tietz, F. “Evaluation of La-Sr-Co-Fe-O Perovskites for Solid Oxide Fuel Cells and Gas Seperation Membranes”, *Solid State Ionics*, **2000**, *135*, 719-725.
4. Ishihara, T.; Arikawa, H.; Akbay, T.; Nishiguchi, H.; Takita, Y. “Nonstoichiometric $La_{2-x}GeO_{5-\delta}$ Monoclinic Oxideas as a New Fast Oxide Ion Conductor”, *Journal of the American Chemical Society*, **2001**, *123*, 203-209.
5. Teraoka, Y.; Zhang, H.-M.; Furakawa, S.; Yamazoe, N. “Oxygen Permeation Through Perovskite-Type Oxide”, *Chemistry Letters*, **1985**, *12*, 1743-1746.
6. Tai, L.-W.; Nasrallah, M. M.; Anderson, H. U. “Thermochemical Stability, Electrical Conductivity, and Seebeck Coefficient of Sr-Doped $LaCo_{0.2}Fe_{0.8}O_{3-\delta}$”, *Journal of Solid State Chemistry*, **1995**, *118*, 117-124.
7. Zeng, Y.; Lin, Y. S.; Swartz, S. L. “Perovskite-Type Ceramic Membrane: Synthesis, Oxygen Permeation and Membrane Reactor Performance for Oxidative Coupling of Methane”, *Journal of Membrane Science*, **1998**, *150*, 87-98.
8. Tan, L.; Gu, X. H.; Yang, L.; Jin, W. Q.; Zhang, L. X.; Xu, N. P. “Influence of Powder Synthesis Methods of $Ba_{0.5}Sr_{0.5}Co_{0.8}Fe_{0.2}O_{3-\delta}$ Perovskite-Type Membrane”, *Journal of Membrane Science*, **2003**, *212*, 157-165.
9. Tan, L.; Gu, X. H.; Yang, L.; Zhang, L. X.; Wang, C. Q.; Xu, N. P. “Influence of Sintering Condition on Crystal Structure, Microstructure, and Oxygen

Permeability of Perovskite-Related Type $Ba_{0.8}Sr_{0.5}Co_{0.2}Fe_{0.2}O_{3-\delta}$", *Separation and Purified Technology*, **2003**, *32*, 307-312.

10. Tejuca, L. G., Fierro, J. L. G. Properties and Applications of Perovskite-type Oxides, New York, Marcel Dekker, Inc., 1p, **1993**.
11. Matsumoto, Y.; Manabe, H.; Sato, E. "Oxygen Evolution on $La_{1-x}Sr_xCoO_3$ Electrodes in alkaline solutions", *Journal of the Electrochemical Society*, **1980**, *127*, 811-814.
12. Teraoka, Y.; Zhang, H. M.; Yamazoe, N. "Oxygen-Sorptive properties of Defect Perovskite-Type $La_{1-x}Sr_xCo_{1-y}Fe_yO_{3-\delta}$", *Chemistry Letters*, **1985**, *9*, 1367-1370.
13. Teraoka, Y.; Furukawa, S.; Zhang, H. M.; Yamazoe, N. "Oxygen Permeability of $La_{1-x}Sr_xCo_{1-y}Fe_yO_{3-\delta}$ Perovskite-Type Oxides", *Journal of the Chemical Society Japan*, **1988**, *7*, 1084-1090.
14. Zhang, H. M.; Shimizu, Y.; Teraoka, Y.; Miura, N.; Yamazoe, N. "Oxygen Sorption and Catalytic Properties of $La_{1-x}Sr_xCo_{1-y}Fe_yO_3$ Perovskite-Type oxides", *Journal of Catalysis*, **1990**, *121*, 432-440.
15. Teraoka, Y.; Nobunaga, T.; and Yamazoe, N. "Effect of Cation Substitution on the Oxygen Semipermeability of Perovskite-type Oxide", *Chemistry Letters*, **1988**, 503-506.
16. Stevenson, J. W.; Armstrong, T. R.; Carmein, R. D.; Pederson, L. R.; Weber, L. R. "Electrochemical Properties of Mixed Conducting Perovskites $La_{1-x}M_xCo_{1-y}Fe_yO_{3-\delta}$ (M = Sr, Ba, Ca)", *Journal of the Electrochemical Society*, **1996**, *143*, 2722-2729.
17. Weller, M. T. Inorganic Materials Chemistry, New York, Oxford University Press Inc, 38p, **1994**.
18. Murray, E. P. R.; Sever, M. J.; Barnett, S. A. "Electrochemical Performance of (La, Sr)(Co, Fe)O_3-(Ce, Gd)O_3 Composite Cathodes", *Solid State Ionics*, **2002**, *148*, 27-34.
19. Wang, W. S.; Virkar, A. V. "A Conductimetric Humidity Sensor Based on Proton Conducting Perovskite Oxides", *Sensors and Actuators B: Chemical*, **2004**, *98*, 282-290.

20. Peña, M. A.; Fierro, J. L. G. "Chemical Structures and Performance of Perovskite Oxides", *Chemical Reviews*, **2001**, *101*, 1981-2017.

21. Goodenough, J. B.; Longo J. M. Crystallographic and Magnetic Properties of Perovskite and Perovskite-related Compounds, Landholt-Bornstein Numerical Data and Functional Relationships in Science and Technology New Series Group III/vol. 4a, Spinger-Verlag, Berlin-Heiderberg, **1970**.

22. Alcock, C. B.; Carberry, J. J.; Doshi, R.; Gunasekaran, N. "Methane Coupling Reaction on Oxide Solid Solution Catalysts", *Journal of Catalysis*, **1993**, *143*, 533-538.

23. Gschneider, K. A. Jr.; Eyring, L. Handbook of the Physics and Chemistry of Rare Earths, Amsterdam, North-Holland Publishers, p553, **1979**.

24. Rao, C. N. R.; Gopalakrishnan, J.; Vidyasagar, K. "Superstructure, Ordered Defects and Nonstoichiometry in Metal Oxides of Perovskite and Related Structure", *Indian Journal of Chemistry*, **1984**, *23A(4)*, 265-284.

25. Tejuca, L. G., Fierro, J. L. G. Properties and Applications of Perovskite-type Oxides, New York, Marcel Dekker, Inc., 3p, **1993**.

26. Yamazoe, N.; Teraoka, Y.; Seiyama, T. "TPD and XPS Study on Thermal Behavior of Adsorbed Oxygen in $La_{1-x}Sr_xCoO_3$", *Chemistry Letters*, **1981**, 1767.

27. Yokoi, Y.; Uchida, H. "Catalytic Activity of Perovskite-Type Oxide Catalysts for Direct Decomposition of NO: Correlation Between Cluster Model Calculations and Temperature-Programmed Desorption Experiments ", *Catalysis Today*, **1998**, *42*, 167-174.

28. Cui, X. L.; Lui, Y.; "New Methods to Prepare Ultrafine Particles of Some Perovskite-Type Oxides", *Chemical Engineering Journal*, **2000**, *78*, 206-207.

29. Zhang, K.; Yang, Y. L.; Ponnunsamy, D.; Jacobson, A. J.; Salama, K. "Effect of Microstructure on Oxygen Permeation in $SrCo_{0.8}Fe_{0.2}O_{3-\delta}$", *Journal of Materials Science*, **1999**, *34*, 1367-1372.

30. Qi, X. W.; Lin, Y. S.; Swartz, S. L. "Electric Transport and Oxygen Properties of Lanthanum Cobalite Membranes Synthesized by Different Methods", *Industrial and Engineering Chemistry Research*, **2000**, *39*, 646-653.

31. Reed, J. S. Introduction of the Principles of Ceramic Processing, John-Wiley & Sons, New York, **1985**.
32. Stewart, G. H. Science of Ceramics, U. K., The British Ceramic Society, Stoke-on Trent, p79-90, **1968**.
33. Onoda, G. Y.; Hench, Jr. L. L. Ceramic Processing before Firing, Wiley, New York, p125-139, **1978**.
34. Johnson, D. W. "Sol-gel Processing Ceramics and Glass", *American Ceramic Society Bullatin*, **1985**, *64(12)*, 1597-1602.
35. Pechini, M. Method of Preparing Lead and Alkaline-earth Titanates and Niobates and Coating Method Using the Same to Form a Capacitor, U. S., **1976**.
36. Baythoun, M. S. G.; Sale, F. R. "Production of Strontium-Substituted Lanthanum Manganite Perovskite Powder by the Amorphous Citrate Process", *Journal of Materials Science*, **1982**, *17*, 2757-2769.
37. Blank, D. H. A.; Kruidhof, H.; Flokstra, J. "Preparation of $YBa_2Cu_3O_{7-\delta}$ by Citrate Synthesis and Pyrolysis", *Journal of Physics. D: Applied Physics*, **1988**, 21, 226-227.
38. Chick, L. A. "Synthesis of Oxide Ceramic Powders by the Glycine-Nitrate Process", *Material Letters*, **1990**, *10*, 1-2.
39. Teraoka, Y.; Kakebayashi, H.; Taura, Y.; Moriguchi, I.; Kagawa, S. Malic "Acid-Aided Synthesis of Perovskite Type Oxides of the La-Co and La-Mn Systems and Their Catalytic Property", *Kidorui*, **1997**, *30*, 124-125.
40. Suresh, K.; Panchapagesan, T. S.; Patil, K. C. "Synthesis and Properties of $La_{1-x}A_xFeO_3$", *Solid State Ionics*, **1999**, *126*, 299-305.
41. Richerson, D. W. Modern Ceramic Engineering, Properties, Processing, and Use in Design, 2nd ed., p378-381, **1992**.
42. Kuczynski, G. C. "Transactions of the American Institute of Mining, Metallurgical, and Petroleum Engineering", *Journal of Applied Physics*, **1950**, *21*, 632-637.
43. Hassel, V. B. A.; Kawada, T.; Sakai, N.; Yokokawa, H.; Dokiya, M.; Bouwmeester, H. J. M. "Oxygen Permeation Modeling of Perovskites", *Solid State Ionics*, **1993**, *66*, 295-305.

44. Waller, D.; Lane, J. A.; Kilner, J. A.; Steele, B. C. H. “The Effect of Thermal on the Resistance of LSCF Electrodes on Galdolinia Doped Ceria Electrolytes”, *Solid State Ionic*, **1996**, *86-88*, 762-772.

45. Roth, R. S. “Classification of Perovskite and Other ABO_3-Type Compounds”, *Journal of Research of the National Bureau of Standards*, **1957**, *58*, 75-88.

46. Tai, L.-W.; Nasrallah, M. M.; Anderson, H. U.; Sparlin, D. M.; Sehlin, S. R. “Structure and Electrical Properties of $La_{1-x}Sr_xCo_{1-y}Fe_yO_{3-\delta}$ Part 1 the System $La_{0.8}Sr_{0.2}Co_{1-y}Fe_yO_{3-\delta}$”, *Solid State Ionics*, **1995**, *76*, 259-271.

47. Tai, L.-W.; Nasrallah, M. M.; Anderson, H. U.; Sparlin, D. M.; Sehlin, S. R. “Structure and Electrical Properties of $La_{1-x}Sr_xCo_{1-y}Fe_yO_{3-\delta}$ part 2 the System $La_{1-x}Sr_xCo_{0.2}Fe_{0.8}O_{3-\delta}$”, *Solid State Ionics*, **1995**, *76*, 273-283.

APPENDIX

APPENDIX

APPENDIX A

Tolerance number

Goldschmidt (1926) defined the tolerance limits of the size of ions through a tolerance factor, t as Equation (A.1)

$$t = (r_A + r_O)/ [\sqrt{2} (r_B + r_O)] \qquad \text{(A.1)}$$

where r_A, r_B, and r_O are the radii of respective ions. For the substituted perovskite at A and B site, $A_{1-x}A'_xB_{1-y}B'_yO_{3-\delta}$, r_A and r_B were calcuated from the sum of each metal at A site and B site, respectively, time its compostition. The atomic weight, ionic charge, coordination number, and ionic radius of all concerned metals were shown in Table A.1

Table A.1 Atomic weight, ionic charge, coordination number, and ionic radius of concerned metals

Metal	Atomic weight	Ionic charge	Coordination No.	Ionic radius (Å)
La	138.92	3+	12	1.36
Fe	55.85	3+	6	0.55
Ba	137.36	2+	12	1.61
Sr	87.62	2+	12	1.44
Co	58.94	2+	6	0.65
O	16.00	2-	6	1.40

Therefore, as Equation A.1 the tolerance number of perovskite compounds such as LSGF 6428 was calculated as below.

$$\text{tolerance number of LSCF8264} = \frac{(1.36 \times 0.8) + (1.44 \times 0.2) + 1.40}{\sqrt{2}\,[(0.65 \times 0.8) + (0.62*0.2)+1.40]}$$

$$= 1.43$$

APPENDIX B

The calculation of the oxygen deficiency at room temperature

The deficiency of oxygen in mole formula, δ, is calculated from the difference of the total charge of oxygen and metals divided by charge of oxygen.

For example, δ of $La_{0.8}Sr_{0.2}Co_{0.6}Fe_{0.4}O_{3-\delta}$, is

$$\delta = \frac{\text{charge of oxygen x mole ratio} - \text{charge of metal in perovkite x mole ratio}}{\text{charge of oxygen atom}}$$

$$= \frac{(3 \times 2) - [(3 \times 0.8) + (2 \times 0.2) + (2 \times 0.6) + (3 \times 0.4)]}{2}$$

$$= 0.4$$

Hence, Oxygen content in LSCF8264 $(3-\delta)$ = 3-0.4

= 2.6

VITAE

Mr. Nitiphong Jirathiwathanakul was born on November 27, 1981 in Suphanburi. He received the B.Sc. Degree in Chemistry at Chulalongkorn University in 2002. Since then, he has been a graduate student studying in Chemistry, Faculty of Science, Chulalongkorn University.

His present address in 28 Moo 2, Samchuk, Samchuk, Suphanburi, 72130, Thailand.